Li, Ying; Chen, Dongdong; Xu, Xin; Wang, Xinyu; Kang, Running; Fu, Mingli; Guo, Yanbing; Chen, Peirong; Li, Yongdan; Ye, Daiqi

# Cold-Start $NO_x$ Mitigation by Passive Adsorption Using Pd-Exchanged Zeolites: From Material Design to Mechanism Understanding and System Integration

*Published in:*
Environmental Science and Technology

*DOI:*
10.1021/acs.est.2c06207

Published: 07/03/2023

*Document Version*
Peer-reviewed accepted author manuscript, also known as Final accepted manuscript or Post-print

# Cold-start $NO_x$ mitigation by passive adsorption using Pd-exchanged zeolites: from material design to mechanism understanding and system integration

Ying Li,[†] Dongdong Chen,[†] Xin Xu,[†] Xinyu Wang,[†] Running Kang,[‡] Mingli Fu,[†] Yanbing Guo,[§] Peirong Chen,[†,*] Yongdan Li,[‡] and Daiqi Ye[†]

[†] *National Engineering Laboratory for VOCs Pollution Control Technology and Equipment, Guangdong Provincial Key Laboratory of Atmospheric Environment and Pollution Control, School of Environment and Energy, South China University of Technology, 510006 Guangzhou, China.*

[§] *Institute of Environmental and Applied Chemistry, College of Chemistry, Central China Normal University, 430079 Wuhan, China.*

[‡] *Department of Chemical and Metallurgical Engineering, School of Chemical Engineering, Aalto University, 02150 Espoo, Finland.*

* Corresponding author. Tel.: +86 (0)20 39380508. E-mail: chenpr@scut.edu.cn.

**Abstract:** It remains a major challenge to abate efficiently the harmful nitrogen oxides ($NO_x$) in low-temperature diesel exhausts emitted during the cold-start period of engine operation. Passive $NO_x$ adsorbers (PNA), which could temporarily capture $NO_x$ at low temperatures (below 200 °C) and release the stored $NO_x$ at higher temperatures (normally 250–450 °C) to downstream selective catalytic reduction unit for complete abatement, hold promise to mitigate cold-start $NO_x$ emissions. In this review, recent advances in material design, mechanism understanding and system integration are summarized for PNA based on palladium-exchanged zeolites. Firstly, we discuss the choices of parent zeolite, Pd precursor and synthetic method for the synthesis of Pd-

zeolites with atomic Pd dispersions, and review the effect of hydrothermal aging on the properties and PNA performance of Pd-zeolites. Then, we show how different experimental and theoretical methodologies can be integrated to gain mechanistic insights into the nature of Pd active sites, the $NO_x$ storage/release chemistry, as well as the interactions between Pd and typical components/poisons in engine exhausts. This review also gathers several novel designs of PNA integration into modern exhaust after-treatment systems for practical application. At the end, we discuss the major challenges, as well as important implications, for the further development and real application of Pd-zeolite-based PNA in cold-start $NO_x$ mitigation.

**Keywords:** Pd-zeolite; passive $NO_x$ adsorber; cold-start; $NO_x$ mitigation; mechanism

**Table of Contents graphic:**

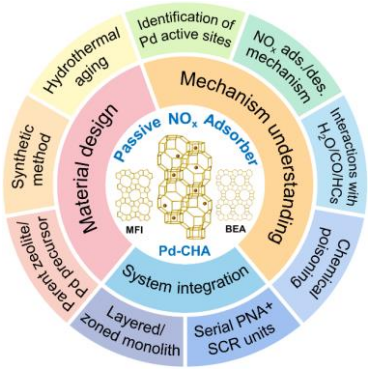

## 1 Introduction

Lean-burn diesel engines are widely used in various stationary equipment and commercial transport vehicles, due to their higher output torque, higher thermal efficiency, better fuel economy and lower $CO_2$ emission than stoichiometrically operated gasoline counterparts.[1–3] However, the environmental impact of diesel engine application has arisen increasing concern, because of the emission of carbon monoxide (CO), hydrocarbons (HCs), particulate matter (PM), nitrogen oxides ($NO_x$), *etc*.[4–6] In particular, $NO_x$ emitted from diesel exhausts account for a large fraction of anthropogenic $NO_x$ emissions and are difficult to be reduced under lean conditions (*i.e.*, with excess oxygen) at low exhaust temperatures.[7–9]

Up to now, exhaust gas recirculation (EGR), lean $NO_x$ trap (LNT), and selective catalytic reduction (SCR) have been successfully developed and applied to $NO_x$ emission control.[10–13] Markedly, SCR using ammonia as a reductant ($NH_3$-SCR) has been widely deployed in after-treatment systems of heavy-duty diesel vehicles to meet the increasingly stringent emission legislations.[14,15] Even though $NH_3$-SCR is highly effective for $NO_x$ abatement above 200 °C, its efficiency is unsatisfactory at lower exhaust temperatures during the "cold-start" period, *i.e.*, the first 100–200 s of engine operation.[16,17] One promising strategy is to adsorb $NO_x$ at low temperatures and desorb the stored $NO_x$ at high temperatures where $NH_3$-SCR catalysts are operational. The corresponding materials for such $NO_x$ storage/release are called passive $NO_x$ adsorbers (PNA).[18–20]

Common PNA materials are noble metals (especially platinum group metals such as Pt, Pd, Rh or Ru) loaded on oxides (*e.g.*, $Al_2O_3$, $CeO_2$ or $CeO_2$-$ZrO_2$) or zeolites (*e.g.*, MFI, BEA, FER or CHA).[21–25] Among others, zeolite-based catalysts stand out due to their lower tendency to form stable nitrates (which are the dominant storage forms of

63 $NO_x$ on $Al_2O_3$-based catalysts and require high temperatures for decomposition)[21,22] and
64 lower susceptibility to sulfur poisoning (which is a problematic issue for $CeO_2$-based
65 catalysts).[24,26] Pt-exchanged zeolites were first extensively investigated as the primary
66 PGM-based zeolite catalysts in PNA,[27–29] and were soon proved to deactivate readily
67 under thermal treatment above 400 °C owing to Pt agglomeration.[30,31] On the contrary,
68 Pd-zeolites can survive under typical harsh conditions of real engine exhausts.[30,32–35]
69 Additionally, Pd-zeolites also demonstrate excellent $NO_x$ storage capacity, suitable $NO_x$
70 desorption temperatures, high (hydro)thermal stability and outstanding resistance to
71 poisoning induced by $SO_2$ and $H_2O$,[25,30,32,33,36] and are thus considered as the most
72 promising material for PNA applications.

73 Zeolites with different framework topologies, including CHA, BEA, MFI, LTA,
74 FER, *etc*., have been explored as PNA materials after Pd exchange.[24–26,32–34,36,37] As
75 compared to Pd-BEA and Pd-MFI, small-pore Pd-SSZ-13 (with CHA framework)
76 shows lower $NO_x$ adsorption capacity and higher $NO_x$ desorption temperature in the
77 feed gas imitating realistic diesel exhausts.[20,24] Even though, Pd-SSZ-13 remains the
78 most promising zeolite material for PNA applications owing to its high HC-poisoning
79 resistance and outstanding hydrothermal stability.[25,36,38,39] It is generally believed that a
80 low Pd loading (< 1 wt.%) is essential for the formation of isolated Pd ions,[40] which are
81 recognized as the active sites for low-temperature $NO_x$ storage.[33] Recently, Khivantsev
82 *et al.*[30] reported that they achieved atomic dispersion of Pd in SSZ-13 at a high Pd
83 loading up to 1.9 wt.%, using a "modified ion-exchange" method and $NH_4$-SSZ-13 (Si-
84 to-Al ratio of 6) as the parent zeolite. While conventional synthesis methods (such as
85 wet impregnation) easily lead to PdO aggregates as the main Pd species on zeolites,
86 post-synthesis treatments (*e.g.*, hydrothermal aging,[32] sequential reduction and re-
87 oxidation[41,42]) are capable of transforming PdO to $Pd^{2+}$. During operation, co-existing

88 components in diesel exhausts, namely $H_2O$, CO and HCs, interact with Pd sites and
89 affect, positively or negatively, the PNA performance of Pd-zeolites.[30,43–45] Notably,
90 while the co-existence of CO could alleviate considerably the inhibition effect of $H_2O$
91 on the $NO_x$ adsorption over Pd-zeolites at low-temperatures, the reduction of Pd ions to
92 metallic Pd by CO at high temperatures may lead to irreversible loss of $NO_x$ storage
93 capacity during cyclic PNA tests.[46]

94 The great promise of PNA in cold-start $NO_x$ mitigation has triggered a research
95 boom in the last five years, and the progress in Pd-zeolite synthesis and $NO_x$
96 adsorption/desorption chemistry has been already documented previously.[26,47,48]
97 Strikingly, significant progress, ranging from the design of Pd-zeolites, mechanism
98 understanding of $NO_x$ adsorption/desorption, to the PNA integration into modern diesel
99 after-treatment systems, has been achieved in the recent two years. This review is
100 intended to provide a comprehensive overview of the very recent updates and existing
101 challenges in this research field. Specifically, the influence of material properties,
102 synthetic methods and post-synthesis treatments on the formation of ionic Pd sites in
103 zeolite matrices are discussed firstly. Then, we introduce briefly the methods for the
104 identification of Pd active sites and the tracking of Pd speciation, describe basic $NO_x$
105 adsorption/desorption mechanism and analyze the interactions between Pd active sites
106 and the typical components and poisons in diesel exhausts. Different configurations of
107 exhaust purification systems integrating PNA are exhibited as well. Finally, we discuss
108 the major challenges and implications for real application of Pd-zeolite-based PNA in
109 cold-start $NO_x$ mitigation.

## 2 Material design

### 2.1 Parent zeolite and Pd precursor

*2.1.1 Zeolite framework*

Zeolite framework is considered as one of the important factors determining the $NO_x$ storage/release performance of Pd-zeolites, and a number of zeolites with pore size ranging from small (8-membered ring; 8MR) to large (12-membered ring; 12MR) have been explored as supports for hosting Pd. Among others, CHA, MFI, and BEA are the most frequently investigated ones.[20,24] Their structural properties are compared in **Table 1** and framework images are illustrated in **Figure 1**, along with other kinds of commonly used zeolites in PNA applications.[49–53]

**Table 1.** Structural properties of zeolites with different topologies

| Framework type | Material name | Dimensionality | Ring types | Limiting pore sizes/Å |
|---|---|---|---|---|
| CHA | SSZ-13<br>SAPO-34 | 3D | 8/6/4 | 3.8×3.8 (8MR) |
| MFI | ZSM-5 | 3D | 10/6/5/4 | 5.3×5.6 (10MR) |
| BEA | Beta | 3D | 12/6/5/4 | 6.6×6.7 (12MR) |
| LTA | LTA | 3D | 8/6/4 | 4.1×4.1 (8MR) |
| FER | Ferrierite | 2D | 10/8/6/5 | 4.2×5.4 (10MR) |

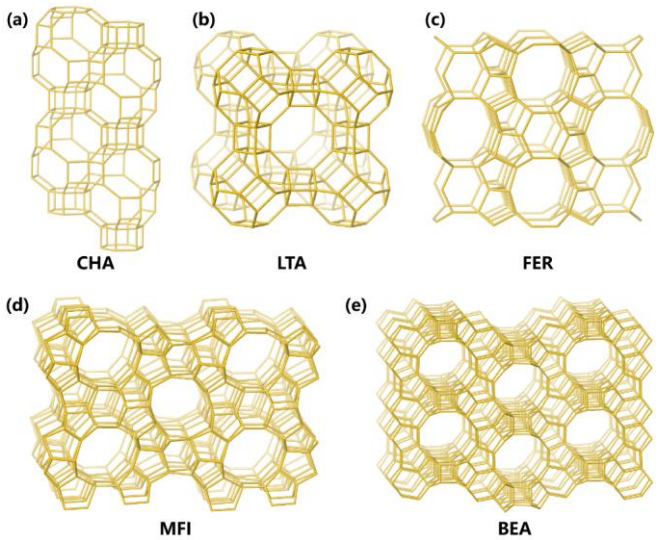


**Figure 1.** Framework images of (a) CHA, (b) LTA, (c) FER, (d) MFI and (e) BEA (obtained from the International Zeolite Association).

124 Chen *et al.*[24] compared the PNA performance of three Pd-zeolites with varied
125 framework structures (*i.e.*, BEA, MFI, CHA) under gas feeds simulating realistic diesel
126 exhausts (at 100 °C), and recorded $NO_x$ storage capacities corresponding to $NO_x$/Pd
127 molar ratios of 0.52, 0.62 and 0.68 for Pd-CHA, Pd-MFI and Pd-BEA, respectively. As
128 for $NO_x$ release, the larger the zeolite pore size, the lower the temperature, the higher
129 the intensity, and the narrower the width of $NO_x$ desorption peak.[24] By means of infrared
130 spectroscopy, the authors also revealed that the binding strength of NO with $Pd^{2+}$ in
131 large-pore zeolite was weaker than that in small-pore zeolite.[24] By contrast, Zheng *et*
132 *al.*,[20] who observed analogous $NO_x$ release trend as above,[24] recorded similar NO
133 binding energies in the three zeolites, and thus assigned the difference in release
134 temperature to varied $NO_x$ diffusion levels in zeolite pores and channels.

135 In terms of $NO_x$ storage capacity, Pd-SSZ-13 seems to be the poorest catalyst,
136 because it has the lowest density of isolated $Pd^{2+}$ as compared to other Pd-zeolites with
137 larger pore sizes.[20,40] However, it is commonly accepted that Pd dispersion is promoted
138 in SSZ-13 because of its strongest Brønsted acidity among the three zeolites.[41,54,55] The
139 low density of isolated $Pd^{2+}$, therefore, can be ascribed to the poor accessibility of
140 exchange sites due to the smallest pore size of SSZ-13. Surprisingly, exploration of Pd-
141 SSZ-13 as PNA catalyst is being intensified in the last few years,[30,42,56–58] because the
142 excellent hydrothermal stability, low Pd mobility, and satisfactory $NO_x$ storage stability
143 over a relatively wide temperature range (80–180 °C) render Pd-SSZ-13 an
144 exceptionally high potential for real application.[24,25,36,59] Even though, solutions must
145 be figured out to sustain the high dispersion of Pd active sites in SSZ-13 at relatively
146 high Pd densities and under harsh conditions.

147 Inspired by the remarkable hydrothermal stability of Cu ion-exchanged LTA
148 (Linde type A) zeolite in $NH_3$-SCR reactions,[52,60] Wang *et al.* also explored the

149 performance and hydrothermal stability of Pd-loaded LTA as a novel PNA catalyst.[34]
150 They found that the framework structure of Pd-LTA was damaged less severely than
151 that of Pd-SSZ-13 after aging at 900 °C. Furthermore, the $NO_x$ storage capacity of Pd-
152 LTA was sustained to a higher extent than that of Pd-SSZ-13, because the highly
153 dispersed Pd species in Pd-LTA are less likely to migrate and aggregate into inactive
154 bulk $PdO_x$ on the outer surface of zeolite.[34] Recently, Pd-FER has been proved to be a
155 promising PNA catalyst as well.[37] A comparison between Pd-FER and Pd-SSZ-13
156 revealed that, in a simulated exhaust gas containing a high concentration of CO (> 500
157 ppm), Pd-FER exhibits a better $NO_x$ adsorption capacity, more suitable desorption
158 temperature and superior hydrothermal stability than Pd-SSZ-13.[61] Despite the progress,
159 more efforts are needed for the search of new zeolites and on the comparative
160 investigations between novel and conventional zeolites, in order to find out the optimal
161 Pd support for concrete PNA performance in real cold-start applications.

162 *2.1.2 Silicon-to-aluminum ratio (SAR) of zeolite*

163 The SAR of parent zeolite could influence the PNA performance by affecting Pd
164 dispersion. Large particles were found to be dominant in Pd-BEA with a SAR of 300,
165 whereas the particles were much smaller with a better dispersion in Pd-BEA with a
166 SAR of 38.[62] A comparative investigation of 1 wt.% Pd-SSZ-13 zeolites with SARs of
167 6, 12 and 30 leads to the same observation, namely an increase of the size of PdO
168 clusters or nanoparticles with SAR (**Figure 2**a–c).[30] Actually, PdO nanoparticles were
169 even not detectable in Pd-SSZ-13 with a SAR of 6 (**Figure 2**a). In PNA tests (**Figure**
170 **2**d), the amount of stored $NO_x$ increased with the decrease of SAR, achieving $NO_x$/Pd
171 ratios of ~1, 0.87 and 0.3 for Pd-SSZ-13 samples with SARs of 6, 12 and 30,
172 respectively.[30] As for $NO_x$ release, while the desorption temperature of Pd-SSZ-13 with
173 a SAR of 12 was slightly lower than that of Pd-SSZ-13 with a SAR of 6, $NO_x$ desorption

was hardly noticeable in case of Pd-SSZ-13 with a SAR of 30 due to a low $NO_x$ adsorption (**Figure 2**d).[30]

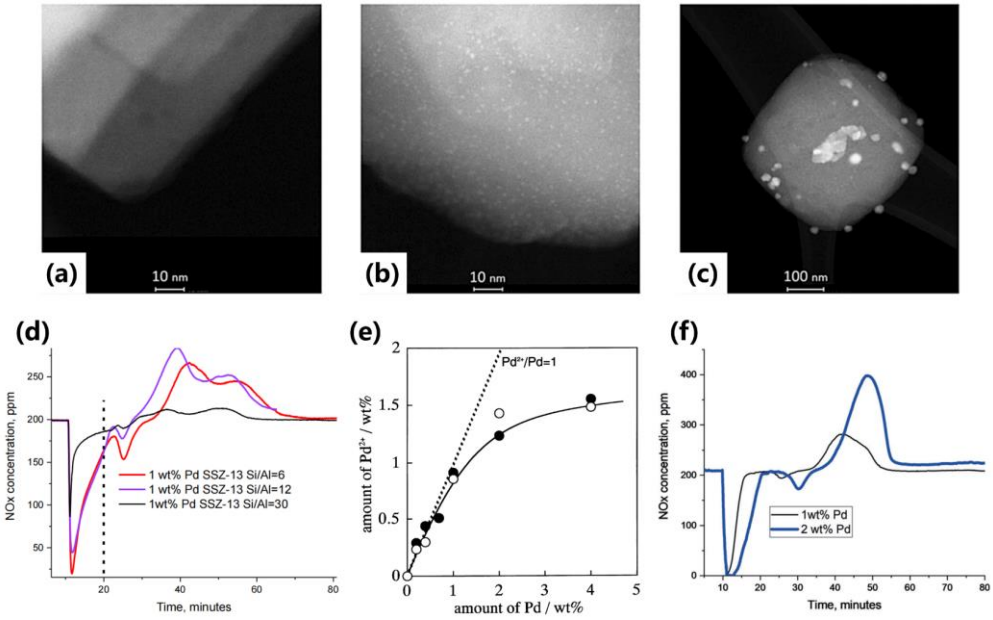


**Figure 2.** HAADF-STEM images of 1 wt.% Pd-SSZ-13 with a SAR of (a) 6, (b) 12 and (c) 30, and (d) corresponding $NO_x$ adsorption/desorption profiles in PNA tests. Reproduced with permission from ref 30. Copyright 2018 Wiley-VCH. (e) Amount of $Pd^{2+}$ in Pd-H-ZSM-5 determined by NaCl titration (solid dots: fresh catalysts calcined at 500 °C; empty circles: after reaction in 1000 ppm $NO_2$, 2000 ppm $CH_4$ and 10 vol.% $O_2$ at 400 °C). Reproduced with permission from ref 40. Copyright 1999 Elsevier. (f) $NO_x$ adsorption/desorption profiles in PNA tests over 1 wt.% and 1.9 wt.% (denoted as 2 wt.%) Pd-SSZ-13 with the same SAR of 6. Reproduced with permission from ref 30. Copyright 2018 Wiley-VCH.

It is well accepted that the anchoring of isolated Pd ions in zeolites is determined by the charge-compensating Al centers on the framework.[58,61,63] Apparently, the higher the Al content (*i.e.*, the lower the SAR) of a zeolite, the higher its ability to accommodate Pd ions. Although Pd dispersion can be promoted by using low-SAR zeolites, the as-formed Pd-zeolite catalysts are subjected to rapid deactivation by the harsh environment in realistic applications.[34,64] Specifically, a higher hydrophilicity of low-SAR zeolite makes Pd species and Brønsted acid sites (BASs, namely the –Al–(OH)–Si– moieties on zeolite framework) more readily affected by $H_2O$, leading to restricted $NO_x$ adsorption.[57,65] Therefore, in some cases, increasing the SAR and

194 hydrophobicity of SSZ-13 by dealumination modification (such as hydrothermal
195 treatment) can alleviate the shielding effect of $H_2O$ on $NO_x$ adsorption, resulting in
196 improved PNA performance.[57] Pertinent details are present in Section 2.3.

197 *2.1.3 Co-cation in zeolite*

198 The use of ammonium ion-exchanged zeolites as starting materials (*e.g.*, $NH_4$-
199 SSZ-13) is critical for achieving high Pd dispersion in Pd-zeolites, as reported
200 repeatedly.[30,58,66] A reversible reaction as shown in Eq. 1 (where $Z^-$ represents the ion-
201 exchange site (*i.e.*, $[–Al–O–Si–]^-$) of a BAS in the zeolite) will take place during the
202 exchange of $Pd^{2+}$ precursors into proton-form zeolites.

203 $$Pd^{2+} + 2\,Z^-H^+ \leftrightarrow Z_2^-Pd^{2+} + 2\,H^+ \quad (1)$$

204 As a result, only a small quantity of $Pd^{2+}$ ions can be accommodated by the ion-
205 exchange sites, whereas a large fraction of $Pd^{2+}$ species fail in the competition with
206 zeolite protons.[30] On the contrary, when using $NH_4$-form zeolite as support and
207 $Pd(NO_3)_2$ or $[Pd(NH_3)_4](NO_3)_2$ as the Pd precursor, the formed $NH_4NO_3$ is prone to
208 decompose at temperatures as low as 180 °C, which facilitates a shift of the reaction
209 equilibrium in Eq. 1 to the right side.[30] Thereby, Pd-zeolite catalysts with more $Pd^{2+}$
210 can be attained. Zhao *et al.*[58] investigated the chemistry during impregnation and
211 calcination of Pd-SSZ-13 prepared using $Pd(NO_3)_2$ and $NH_4$-SSZ-13, and proposed that
212 $Pd(NO_3)_2$, which remained intact after impregnation, was transformed into highly
213 mobile $Pd(NH_3)_x^{2+}$ during calcination at 200–290 °C. The subsequent oxidation of $NH_3$
214 ligands to $N_2$ at 290–450 °C led to $Pd^{2+}$ sites anchored to the zeolite framework. Notably,
215 more compelling evidence is still needed to understand the formation and dynamic of
216 $Pd(NH_3)_x^{2+}$, because multiple metal–$NH_3$ complexes can be easily formed upon the
217 interaction between metal ions and $NH_3$ ligands, as showcased by Cu-SSZ-13 for $NH_3$-
218 SCR catalysis.[67]

219 The impact of other co-cations (*e.g.*, $Na^+$ or $K^+$) on the performance of Pd-zeolites
220 is yet to be clarified. Ryou *et al.* reported that $NH_4$-SSZ-13 pre-exchanged with $NaNO_3$
221 or $KNO_3$ as a support led to significantly reduced $NO_x$ storage capacity of the resultant
222 Pd-SSZ-13,[68] whereas Li *et al.* proposed a promotion mechanism of Na co-cations on
223 hydrothermal stability and $NO_x$ adsorption ability of Pd-SSZ-13.[69] On the one hand,
224 BASs could be protected from dealumination by the prior occupation of Na co-cations
225 and then stabilize more $Pd^{2+}$ cations during hydrothermal aging.[69] On the other hand,
226 the occupation of BASs by the pre-exchanged cations may restrict the accessibility of
227 ion-exchange sites for Pd ions.[68]

228 *2.1.4 Crystal size of zeolite*

229 Zeolites of the same topology but with different crystal sizes also present
230 discrepant PNA behaviors. Chen *et al.*[56] obtained Pd-SSZ-13 zeolites with different
231 crystal sizes (0.4, 0.8, and 2.3 μm) by adding distinct amounts of crystal seed during
232 zeolite synthesis. Among the three Pd-SSZ-13 zeolites, the one with the smallest crystal
233 size (0.4 μm) demonstrated the highest $NO_x$ adsorption capacity and most robust
234 hydrothermal stability, which originates from its most abundant acid sites on the
235 framework leading to the highest prosperity of Pd ions.[56] Notably, zeolite with a smaller
236 crystal size does not always perform better in PNA application. For example,
237 Khivantsev *et al.* demonstrated that defect-free Pd-BEA with larger crystals showed
238 higher $NO_x$ storage capacity, more suitable $NO_x$ release temperature and better
239 hydrothermal stability than defective Pd-BEA with nanocrystals.[70] The nanocrystalline
240 Pd-BEA with more defect sites led to an easier deprivation of tetrahedral Al (T-Al) sites
241 (*i.e.*, dealumination) during hydrothermal aging. Consequently, Pd ions, which were
242 initially balanced by T-Al sites, were prone to agglomerate into $PdO_x$ particles on aged
243 Pd-nanoBEA, resulting in poor PNA performance.[70] It has to be pointed out that these

244 Pd-BEA samples also have different Al distributions, and their impact on the Pd
245 distribution within the BEA framework should be considered in future research of Pd-
246 zeolites with varying crystal sizes. The crystal size effect for other zeolites (SAPO-34,
247 ZSM-5, LTA, MOR, FER, and so on), which has already been investigated for various
248 catalytic reactions,[71–75] is awaiting clarification in PNA applications.

249 *2.1.5 Pd precursor and loading*

250 In addition to parent zeolites, Pd precursors used in Pd-zeolite synthesis could
251 influence the PNA performance to different extents as well. Lee *et al.*[57] found that using
252 $Pd(NH_3)_4Cl_2 \cdot H_2O$, instead of $Pd(NO_3)_2 \cdot 2H_2O$, as Pd precursor was more instrumental
253 in achieving a high Pd dispersion, and no PdO particle formation was observed on the
254 resultant Pd-SSZ-13 after different treatments. Similar conclusions were drawn over a
255 series of Pd-SSZ-13 samples prepared using the same Pd precursors, *i.e.*,
256 $Pd(NH_3)_4Cl_2 \cdot H_2O$ and $Pd(NO_3)_2 \cdot 2H_2O$, and two forms of zeolites (*i.e.*, H-SSZ-13 and
257 $NH_4$-SSZ-13).[66]

258 Pd loading is another key factor that influences greatly the PNA performance of
259 Pd-zeolites. While increasing Pd loading is necessary to obtain an increased amount of
260 isolated Pd ions in Pd-zeolites, it inevitably raises the tendency of PdO agglomeration.
261 According to Ogura *et al.*,[40] in a ZSM-5 zeolite with a SAR of ~20, Pd species existed
262 mainly as $Pd^{2+}$ at Pd loadings below 0.7 wt.%. At Pd loadings above 1 wt.%, on the
263 contrary, Pd existed mainly as PdO, and the degree of PdO agglomeration increased
264 with Pd loading (**Figure 2**e). Similarly, Khivantsev *et al.*[30] recorded full Pd utilization
265 (*i.e.*, a NO/Pd ratio of 1) in passive $NO_x$ adsorption over Pd-SSZ-13 (SAR~6) at a Pd
266 loading as high as 1.9 wt.% (**Figure 2**f), and decreased NO/Pd ratios at higher Pd
267 loadings of 3 wt.% and 5 wt.%. Ryou *et al.*[32] also found that the desorbed NO amount
268 from Pd-SSZ-13 (SAR~22) increased with Pd loading up to 2 wt.%, and decreased

269 gradually at higher Pd loadings (3 wt.% and 5 wt.%). Moreover, it was found that the
270 increase of Pd loading also led to an increase of $NO_x$ release temperature.[30]

271 **2.2 Synthetic method**

272 There are several frequently used methods of loading Pd onto/into zeolites,
273 including wet impregnation (WI), incipient wetness impregnation (IWI), ion exchange
274 (IE) and solid-state ion exchange (S-S).[32,33,61] While the IE method ensures a relatively
275 better dispersion of the exchanged Pd species within the zeolite framework, the S-S
276 method avoids liquid-phase chemistry that may generate wastewater. However, a higher
277 energy input is needed in S-S synthesis and may damage the zeolite framework.[76,77] The
278 WI/IWI method assures that all Pd precursors remain on/in the Pd-zeolite product, but
279 may lead to a high fraction of $PdO_x$ particles rather than Pd ions. Recently, it was
280 evidenced that the IWI method, when properly parameterized, is advantageous in the
281 synthesis of high-loading Pd-zeolites with predominant presence of Pd ions.[30]
282 Therefore, there is an increasing number of works employing the IWI method to
283 synthesize high-performance Pd-zeolite catalysts.[34,56,78] For freshly prepared Pd-
284 zeolites by WI, IWI or IE methods, post-synthesis treatments, most commonly
285 calcination, are often needed before use, and were found to affect the PNA performance
286 as well. As an example, slowing the heating rate during calcination led to decreased
287 $PdO_x$ content in the final Pd-SSZ-13 prepared by an IE method,[66] implying that
288 optimizing the calcination parameter is of great potential to improve the ion exchange
289 efficiency in Pd-SSZ-13 synthesis.

290 **2.3 Hydrothermal aging**

291 Hydrothermal aging (HTA), depending on the treatment temperature and Pd
292 distribution in the original material, has varying impacts on the properties and PNA
293 performance of Pd-zeolites. As mentioned in Section 2.1.1, Pd-SSZ-13 possesses a

higher hydrothermal stability than Pd-ZSM-5 and Pd-BEA. More interestingly, the $NO_x$ storage capacity of Pd-SSZ-13 can be further improved after HTA at 750 °C,[57] although it declined after HTA above 800 °C.[34,64] In the work of Lee *et al.*,[57] HTA at 750 °C, while maintaining largely the framework structure and the atomic Pd dispersion, induced dealumination (as indicated by the increase of SAR from 9 to 41 or from 35 to 72) and, consequently, improved the hydrophobicity of Pd-SSZ-13, eventually minimizing the negative impacts of $H_2O$ adsorption on $NO_x$ storage. As a consequence, the catalyst after HTA at 750 °C displayed improved $NO_x$ storage capacity and more favorable $NO_x$ desorption temperature range in PNA tests with $H_2O$.[57]

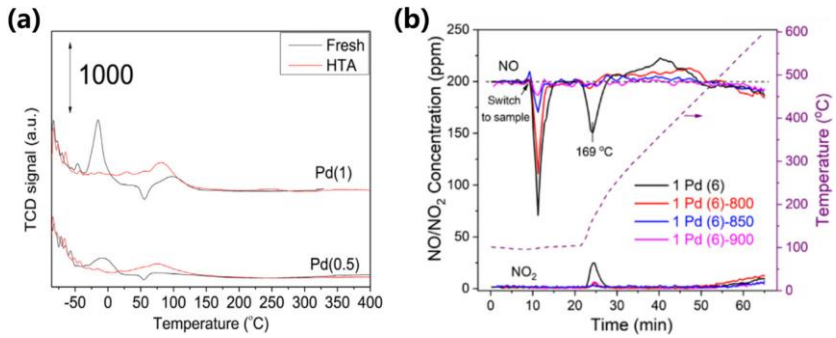


**Figure 3.** (a) $H_2$-TPR profiles of fresh and HTA Pd-SSZ-13 catalysts with a Pd loading of 0.5 wt.% or 1 wt.%. Reproduced with permission from ref 32. Copyright 2017 Elsevier. (b) $NO/NO_2$ profiles in PNA over fresh and HTA Pd-SSZ-13 (SAR~6, 1 wt.% Pd) denoted as 1 Pd (6) and Pd (6)-X (refers to the HTA temperature), respectively. Reproduced with permission from ref 64. Copyright 2020 Elsevier.

In addition to hydrophobicity improvement, HTA treatment at 750 °C can also lead to the redistribution of Pd species.[32,57] As revealed by $H_2$-TPR (**Figure 3**a), HTA treatment led to a dramatic intensity decrease for the PdO reduction peak at *ca.* 0 °C and, meanwhile, an intensity increase of the reduction peak at *ca.* 100 °C for isolated $Pd^{2+}$ ions, suggesting a redispersion of PdO aggregates into $Pd^{2+}$.[32] The negative peak at around 60 °C correlated with the decomposition of Pd hydride, which was formed by reaction of metallic Pd (from PdO reduction) and $H_2$, was weakened after HTA treatment, further confirming a lower PdO content in the HTA Pd-SSZ-13 catalyst.

317 Markedly, these improvements by HTA are believed to occur only on Pd-zeolites with
318 spare Al centers and large $PdO_x$ particles.[32,57]

319 At temperatures above 800 °C, however, HTA was frequently reported to
320 deactivate Pd-zeolites (even the Pd-SSZ-13).[34,36,64] As shown in **Figure 3**b, the PNA
321 performance of Pd-SSZ-13 degraded gradually with the increase of HTA temperature,[64]
322 due to the dealumination of zeolite framework and the agglomeration of isolated Pd
323 ions to PdO particles.[32,34–36,64] A higher SAR could improve the resistance of Pd-zeolites
324 against deactivation by HTA above 800 °C.[64] Compared with Pd-SSZ-13, several newly
325 developed Pd-zeolites, such as Pd-LTA and Pd-AEI,[34,35,78] show significantly higher
326 hydrothermal stability above 800 °C, implying the exceptional potential of these novel
327 zeolites for the preparation of even more robust PNA catalysts.

328 To summarize Section 2, Pd-zeolite catalysts with atomically dispersed Pd active
329 sites can be prepared mainly through two ways. The first one is to improve ion-
330 exchange efficiency between the Pd precursor and the parent zeolite during synthesis,
331 which can be achieved by modified ion-exchange methods (*e.g.*, incipient wetness
332 impregnation) while using large-pore, low-SAR or $NH_4$-form zeolites as the parent
333 zeolite and low-content Pd-ammine compounds as the Pd precursor. Another one is to
334 transform $PdO_x$ aggregates into isolated $Pd^{2+}$ through post-treatments, *e.g.*, HTA
335 treatment at 750 °C. Nevertheless, large-pore and low-SAR zeolites have poor
336 resistance to high-temperature hydrothermal aging, which is one of the important
337 criteria for practical application. In this case, selection of a zeolite with a SAR matching
338 the Pd loading and further modification by post-treatments can also be feasible
339 solutions to obtain atomically dispersed Pd species in hydrothermally stable small-pore
340 zeolites, such as CHA, LTA, AEI, *etc*.

341 **3 Mechanism understanding**

342 **3.1 Identification of Pd active sites**

343 Understanding the nature and dynamics of Pd active sites is conducive to unravel
344 $NO_x$ adsorption/desorption mechanism on Pd-zeolites, and to guide a subtle design of
345 PNA materials with high activity and robust stability. This section gives an overview of
346 the experimental and theoretical methods for identifying the Pd active sites, and of the
347 interconversion of Pd between aggregated and highly dispersed states.

348 *3.1.1 Methodologies*

349 **X-ray based techniques.** Techniques based on highly penetrative X-rays, such as
350 X-ray diffraction (XRD), X-ray absorption near edge structure (XANES) and extended
351 X-ray absorption fine structure (EXAFS), are often applied to characterize
352 heterogeneous catalysts including Pd-exchanged zeolites.[17] Although XRD can be used
353 to detect the bulk PdO phase (at 2θ ~34.0°) in, for example, Pd-zeolites after HTA
354 treatments,[25,33] it is insensitive to the micro-structural changes related to the highly
355 dispersed Pd sites. Pd K-edge XANES and EXAFS (generally $k^3$-weighted Fourier-
356 transformed) are capable of resolving, *off situ* or *in situ*, the oxidation state and
357 coordination environment of Pd species that are active in PNA.[17,54] In XANES spectrum,
358 Pd oxidation states can be judged by comparing with the absorption edge energies and
359 white line intensities of reference materials (*e.g.*, Pd foil and PdO).[66] Note that white
360 line refers to the first resonance peak after the edge.[79] A decrease of Pd valence leads to
361 a shift of the absorption edge to lower energy positions and a decline of white line
362 intensity. For instance, the absorption edge energy of NO-adsorbed sample is lower than
363 that of oxidized sample in **Figure 4**a, assigned to the reduction of $Pd^{2+}$ to $Pd^{+}$ by NO.[54]
364 However, in PNA research, the coordination state of Pd species is rarely analyzed with
365 XANES, which has the potential to testify the formation and variation of diverse Pd

complexes based on the position and intensity of the pre-edge peak.[79]

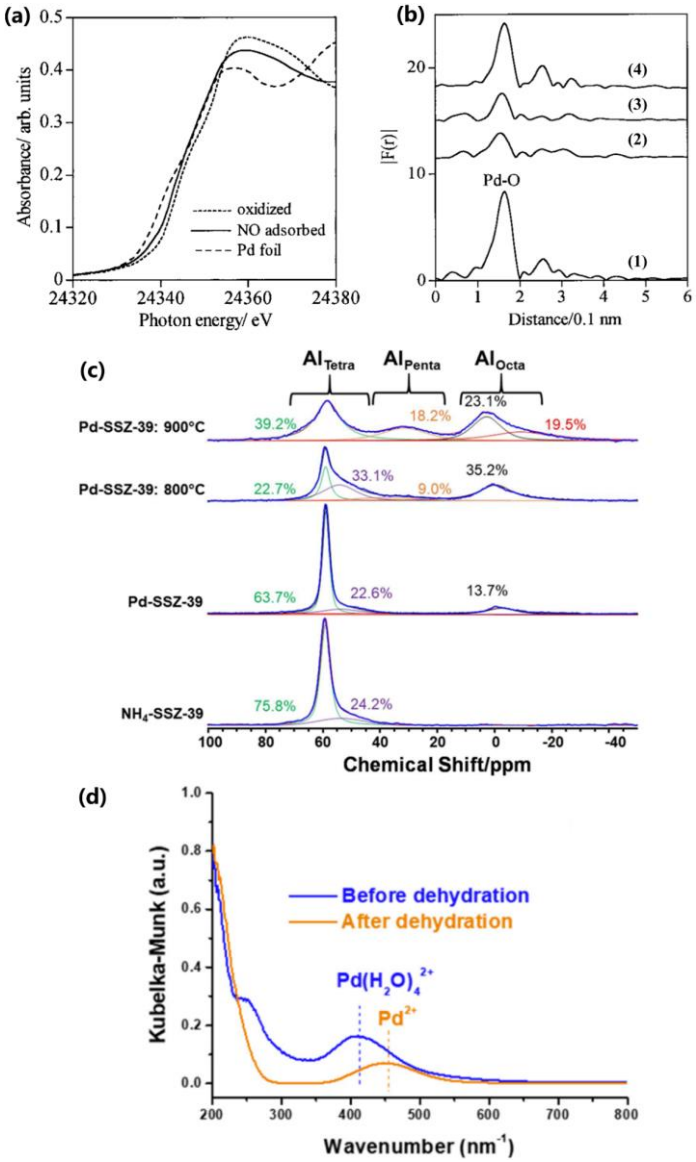


**Figure 4.** (a) Pd K-edge XANES spectra for Pd-ZSM-5 measured before and after NO adsorption at room temperature. (b) Fourier transforms of $k^3$-weighted Pd K-edge EXAFS for Pd-ZSM-5: (1) oxidized at 500 °C; (2) exposed to NO at room temperature and subsequently heated to (3) 100 °C and (4) 400 °C. Reproduced with permission from ref 54. Copyright 2000 American Chemical Society. (c) High-field $^{27}$Al MAS NMR spectra for $NH_4$-SSZ-39, fresh and aged (800/900 °C) Pd-SSZ-39. Reproduced with permission from ref 35. Copyright 2020 Elsevier. (d) UV/vis spectra of Pd-SSZ-13 before and after dehydration at 500 °C. Reproduced with permission from ref 57. Copyright 2020 Elsevier.

Conversely, EXAFS is usually employed to resolve the local structures of Pd sites, including coordination number, ligand type, bond distance, *etc*.[17] The feature at the

378 radial distance of 1.6 Å corresponds to Pd–O bond, which may result from bulk PdO,
379 isolated PdO/$[Pd(OH)]^+$ species, and isolated Pd ions.[80] The peaks at 2.5 Å and 3 Å are
380 attributed to Pd–Pd bonds and Pd–O–Pd bonds, originating from bulk Pd metal and
381 aggregated PdO, respectively.[80,81] Therefore, the type and dispersion of Pd species in
382 zeolites can be determined by the intensities of these features.[66,81] In **Figure 4**b, the
383 decrease in intensity of Pd–O shell after NO exposure signified that NO facilitated the
384 redistribution of Pd species in zeolites.[54]

385 **NMR and optical spectroscopy.** $^{27}$Al magic angle spinning nuclear magnetic
386 resonance ($^{27}$Al MAS NMR) spectroscopy, by detecting the type and distribution of Al
387 species, could provide rich information on the local framework structure of a zeolite
388 and its change by HTA or poisoning.[35,68,69] Attributions of three common Al NMR
389 features in Pd-SSZ-39 are displayed in **Figure 4**c,[35] and are applicable to other types of
390 zeolite as well. The content of T-Al sites, which is generally proportional to the amount
391 of ionic Pd sites in fully ion-exchanged zeolites, will be decreased by HTA treatments
392 and chemical poisoning.[35,64,70] As discussed above, zeolite acidity is defined by
393 framework Al distribution, which has essential impacts on the micro-scale structure and
394 siting position of Pd species, and in turn the PNA performance. When studying the
395 poisoning of Pd-zeolites by P, the interaction of Pd sites and P poisons can be disclosed
396 based on the feature of δ −13 ppm in the $^{31}$P NMR spectrum.[43]

397 The nature (*e.g.*, redox and coordination state) of varying Pd species in Pd-zeolites
398 can be investigated by ultraviolet–visible (UV–vis) spectroscopy, based on the ligand-
399 to-metal charge transfer (LMCT) transitions (200–300 nm) and characteristic *d–d*
400 transitions (300–800 nm) of different Pd species.[24,43,66] Although both $Pd^{2+}$ and
401 $[Pd(OH)]^+$ species in zeolites give rise to strong LMCT bands below 250 nm,[43,57,58] it
402 remains a challenge to resolve the definitive structures of these ionic Pd species by UV–

403 vis alone. There are existing controversies for the ascription of absorbance bands in the
404 visible range of spectrum (400–800 nm). For a freshly prepared Pd-SSZ-13, the band
405 at ~400 nm, which may be derived from $Pd(H_2O)_n^{2+}$, underwent a red shift to the 450–
406 480 nm wavelength region after calcination, likely due to the dehydration of $Pd(H_2O)_n^{2+}$
407 to $Pd^{2+}$ (**Figure 4**d).[57,66,82] Besides, *d–d* transitions of $PdO_x$ particles in calcined samples
408 contribute to the band between 400–500 nm as well.[24,43,58]

409 Fourier transform infrared spectroscopy (FTIR), as one of the most widely used
410 methods for catalyst characterization, is extremely powerful in the identification of
411 storage sites of Pd-zeolites, usually using probe molecules such as NO, CO and $NH_3$ to
412 mimic the reaction conditions.[17,63,64,83,84] In particular, FTIR in diffuse reflection mode,
413 *i.e.*, DRIFTS, allows to work directly on powder-form zeolite catalysts without great
414 sacrifice of sensitivity, accuracy, and resolution.[17] Using NO as a probe, DRIFTS is
415 capable of identifying most $NO_x$ adsorption sites (*e.g.*, BASs, ionic Pd species) in Pd-
416 zeolites under *in situ/operando* environments relevant for PNA application. In the NO-
417 DRIFT spectrum, the feature at ~3600 $cm^{-1}$ represents $\nu$(OH) stretching of BAS groups
418 in Pd-zeolites.[41,83] Pd-nitrosyl species, formed by the interaction between NO and
419 cationic Pd sites, contribute to IR bands in the range of 1900–1800 $cm^{-1}$ (**Figure 5**a).
420 Nonetheless, unanimity is yet to reach for the attribution of these NO stretching features
421 due to the presence of multiple Pd species. CO is also frequently utilized as a probe
422 molecule to detect the oxidation state and coordinative environment of Pd species,
423 because the vibrational frequency of C–O bond is highly sensitive to the surroundings.[85]
424 CO-DRIFT spectra show plenty of vibrational features, among which the peaks above
425 2100 $cm^{-1}$ result from Pd-carbonyl species, such as $Pd^{+}$-CO, $Pd^{2+}$-CO, $Pd^{2+}$-$(CO)_2$ or
426 $Pd^{3+}$-$(CO)_2$.[20,41,83,86] The vibrational features below ~2100 $cm^{-1}$ are related to metallic
427 Pd derived from the reduction of small $PdO_x$ clusters by CO.[58,86] Besides, DRIFTS

could also provide solid evidence for the formation of a bidentate complex $Pd^{2+}$(NO)(CO) by co-adsorption of CO and NO on $Pd^{2+}$ ions.[65,87] Considering the high sensitivity of CO vibrations to the environment, researchers have employed DRIFTS to determine the siting locations of ionic Pd species in/on the framework structure of a zeolite.[43,58,64] The strong Lewis basicity of $NH_3$ makes it readily bonded to various acid sites (*e.g.*, protons and Pd ions) of Pd-zeolites to form $NH_4^+$ and $Pd(NH_3)_x^{2+}$ species.[42,58] Therefore, $NH_3$ is frequently used in DRIFTS to study the bulk acidity of zeolite catalysts and quantity of cationic Pd sites.[42] The interaction between metal ions and the zeolite framework can also be detected by $NH_3$-DRIFTS, according to the metal ion-perturbed T–O–T vibrations in the range of 1000–850 $cm^{-1}$.[58,88] Specifically, $[Pd(OH)]^+$ and $Pd^{2+}$ ions lead to negative IR bands at ~910 $cm^{-1}$ and ~880 $cm^{-1}$, respectively (**Figure 5**b).[43]

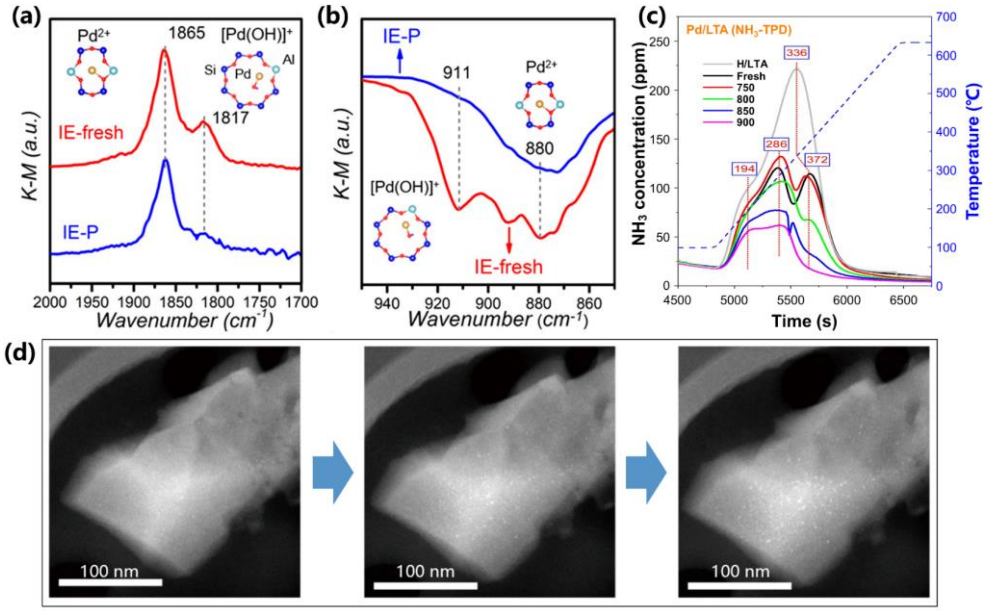


**Figure 5.** *In situ* (a) NO-DRIFT and (b) $NH_3$-DRIFT spectra for the fresh and P-poisoned Pd-SSZ-13 catalysts (denoted as IE-fresh and IE-P, respectively). Reproduced with permission from ref 43. Copyright 2021 American Chemical Society. (c) $NH_3$-TPD profiles for H-LTA, fresh and aged Pd/LTA samples. Reproduced with permission from ref 34. Copyright 2020 Wang *et al*. (d) Serial STEM images of Full-$Pd^{2+}$/SSZ-13 obtained under conventional STEM mode, starting from the initial time period of imaging. Reproduced with permission from ref 66. Copyright 2021 The Royal Society of Chemistry.

448 **Temperature-programmed methods.** Temperature-programmed reduction (TPR)
449 can distinguish Pd species with varying oxidation states via defining their peak
450 positions for reduction to metallic Pd by $H_2$, CO or $CH_4$.[56,89,90] $H_2$ is frequently used as
451 a reductant because of the straightforward reaction between $H_2$ and high-valence Pd.
452 Concrete peak attributions in $H_2$-TPR profiles are described in Section 2.3. Changes in
453 width and position of PdO peak may also be related to diverse particle sizes of
454 PdO.[32,78,91] Temperature-programmed desorption (TPD) is mainly used to investigate
455 the type and abundance of metal sites or acidic sites in Pd-zeolites, based on the
456 interactions between probe molecules (*e.g.*, NO and $NH_3$) and catalysts.[92–94] For
457 example, $NH_3$-TPD can be applied to quantitatively characterize acid sites with diverse
458 strength.[92] In a typical $NH_3$-TPD profile, the high-temperature peak is ordinarily
459 attributed to strong BASs, while the assignments of peaks at low and medium
460 temperatures are still controversial.[34,93,94] Even though the desorption peaks for $NH_3$
461 from Brønsted and Lewis acid sites partially overlap, their contributions can be
462 differentiated by reasonable peak deconvolution. Besides, relative quantity of Pd ions
463 can be derived by comparative $NH_3$-TPD studies over fresh and HTA-treated Pd-
464 zeolites, because Pd sites largely remain in zeolites as Lewis acid sites while most BASs
465 are eliminated after HTA above 750 °C (**Figure 5**c).[34,56]

466 **Electron microscopy.** Transmission electron microscopy (TEM) and scanning
467 electron microscopy (SEM) are among the most commonly utilized tools to observe
468 micro-scale structures and surface morphologies of solid catalysts.[95,96] With respect to
469 Pd-zeolites, the dispersion and particle size of Pd species can be visualized by TEM,
470 whereas typical SEM is only able to display the crystal size and surface morphology of
471 zeolites.[56,64] Scanning transmission electron microscopy (STEM), when equipped with
472 high-angle annular dark-field (HAADF) detector, is extensively adopted to acquire

473 images with atomic resolution (**Figure 2**a–c), and thus increasingly used to visualize
474 the atomically dispersed Pd species in zeolites.[34,46] In cooperation with electron
475 microscopy, energy-dispersive X-ray spectroscopy (EDS) mapping allows to exhibit
476 chemical compositions and their distributions.[89] However, it has been proposed that the
477 high-energy electron beam may induce a collapse of zeolite framework and thus the
478 formation of metal clusters within a few seconds (**Figure 5**d).[30,66] Cryogenic STEM,
479 which can reach a temperature as low as −180 °C, is capable of minimizing the
480 deterioration of electron-beam-sensitive materials during imaging process, thus
481 demonstrating great potential in the visualization of atomically dispersed Pd species in
482 zeolite matrix.[66]

483 **Theoretical simulations.** Pd speciation is fundamentally determined by the nature
484 of Al species in zeolite framework (**Figure 6**a) and by the applied reaction conditions,
485 which can be explored with the aid of theoretical modeling.[63,97] A combination of
486 simulation tools and the above-mentioned characterization techniques enables more
487 practical and accurate interrogation of Pd species throughout the lifetime of Pd-zeolite
488 catalysts. For example, combined experimental and computational analyses by Mandal
489 *et al.* have revealed the optimized geometries of three ionic Pd species, *i.e.*, $Pd^{+}$,
490 $[Pd(OH)]^{+}$, $Pd^{2+}$ and their fully hydrated counterparts in Pd-SSZ-13, as illustrated in
491 **Figure 6**b and **6**c.[63] $Pd^{+}$ and $[Pd(OH)]^{+}$ are charge-compensated by one T-Al site (1Al)
492 at six- and eight-membered rings (6MR and 8MR), respectively, while $Pd^{2+}$ is balanced
493 by a pair of T-Al sites (2Al) at 6MR. The endothermic transition of Pd ions from 2Al
494 to 1Al site demonstrates the preferential formation of $Pd^{2+}$ at 2Al sites within 6MR.
495 Calculations suggest that $Z_2[Pd^{II}(H_2O)_4]$, namely hydrated $Pd^{II}$ coordinated to the 2Al
496 sites of zeolite framework, is the most stable complex at 298 K and under 4.5 vol.%
497 $H_2O$, which will turn back into $[Z_2Pd^{II}]$ after dehydration at high temperatures. Upon

NO storage, site exchange between $Pd^{+}$ and $[Pd(OH)]^{+}$ occurs (**Figure 6**d). Subsequent adsorption of $H_2O$, rather than NO, pushes Pd species away from the zeolite framework. Under NO and $H_2O$, the most stable species is $Z[Pd^{II}(NO^{-})(H_2O)_3]$, a fraction (~10%) of which originates from $Z_2[Pd^{II}(H_2O)_4]$. The $Z[Pd^{II}(NO^{-})(H_2O)_3]$ complex releases NO at a higher temperature than $[ZPd^{I}(NO)]$ and $[Z_2Pd^{II}(NO)]$, which are the most stable adsorbed species in the absence of $H_2O$.[63]

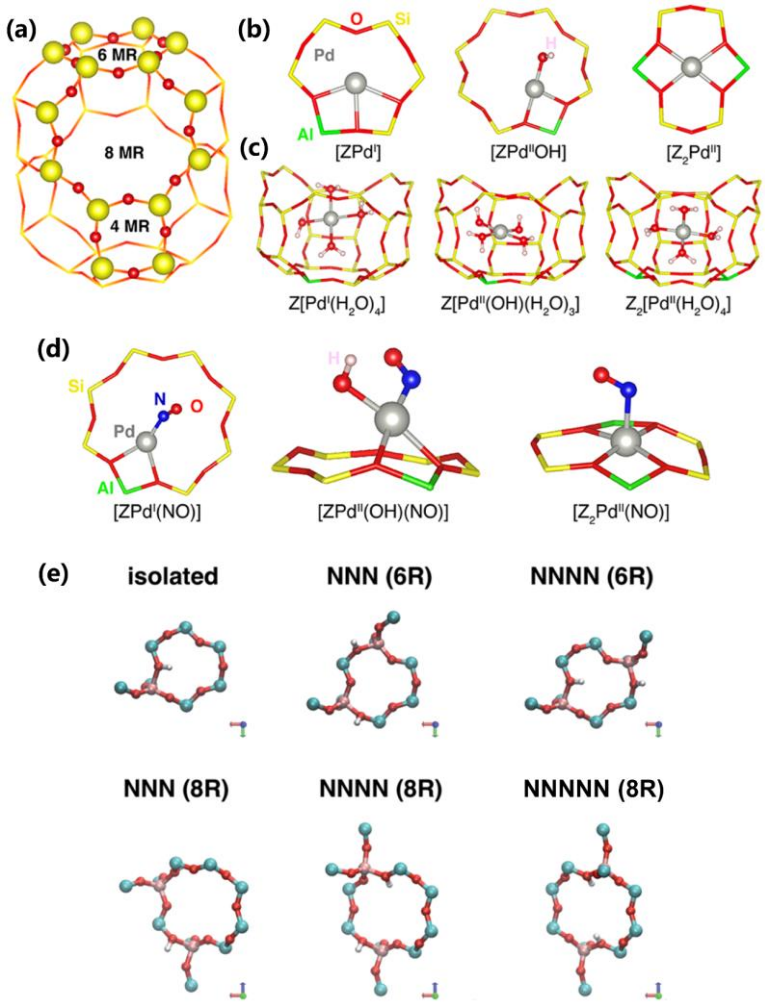


**Figure 6.** (a) Framework of the SSZ-13 cage made up of 4/6/8MR. HSE06-optimized structures of (b) 1Al and 2Al Pd-exchanged sites (Z represents one T-Al site of a BAS in the zeolite), (c) hydrated sites, (d) NO adsorbed on 1Al and 2Al Pd-exchanged sites. Reproduced with permission from ref 63. Copyright 2020 American Chemical Society. (e) QM region-simulated (8–12 T-atoms) active sites at isolated Al and different proximate Al pairs in the 6MR (NNN and NNNN) or 8MR (NNN, NNNN and NNNNN). The atoms are Si (cyan), Al (pink), O (red), H (white). Reproduced with permission from ref 97. Copyright 2021 The Royal Society of Chemistry.

513 Theoretically, 2Al sites also exist in 8MRs of SSZ-13, and may act as the exchange
514 sites of divalent cations as well.[98,99] On the other hand, a consensus over the precise Al
515 arrangements in specific zeolites (even for the structurally simplest CHA zeolite) has
516 not been established up to now. In addition to the 2Al configuration (denoted as a next–
517 next nearest neighbor, *i.e.*, NNNN, which represents the case that two Al atoms are
518 separated by two Si atoms) in **Figure 6**b, 2Al sites in 6MR can be also aligned as next
519 nearest neighbor (NNN) Al pair, namely the two Al atoms are separated by one Si atom.
520 Similarly, 8MR could comprise analogous Al pair sites and even a next–next–next–
521 nearest neighbors (NNNNN) Al pair (**Figure 6**e). A study by Van der Mynsbrugge *et*
522 *al.*[97] suggested that $Pd^{+}$ seems to be the most stable species at all the Al sites in **Figure**
523 **6**e except for the NNNN Al pair in 6MR, which is preferentially occupied by $Pd^{2+}$ under
524 a variety of conditions. It should be noted that the original nature of Pd species is
525 simulated just before the introduction of reaction gas for PNA application in this work.[97]
526 A separate and similar prediction of stability was reported by Aljama *et al.*, who
527 regarded $Pd^{+}$ and $Pd^{+}H^{+}$ as the most stable sites for NO adsorption using a high-
528 throughput screening approach.[100]

529 Recently, Khivantsev *et al.* performed density-functional theory (DFT)
530 calculations to validate their ascriptions of IR bands for multiple adsorbed species,
531 especially the $Pd^{2+}(NO)(CO)$ complex, in the co-existence of CO and NO, and revealed
532 the formation of dimers such as $Pd^{2+}(O)Pd^{2+}$.[30,65] Simulation results also confirmed that
533 ethylene can be readily adsorbed on Pd-carbonyl or Pd-nitrosyl species to form
534 $Pd^{2+}(CO)(C_2H_4)$ or $Pd^{2+}(NO)(C_2H_4)$, providing perspectives on the development of
535 novel materials for simultaneous passive adsorption of CO, NO and HCs.[86]

536 *3.1.2 Pd speciation and transformation*

537 Calcination or other treatments lead to a transformation of Pd precursors to

538 multiple Pd sites, including $Pd^0$, $Pd^I$ ($Pd^+$), $Pd^{II}$ (isolated $Pd^{2+}$ and $[Pd(OH)]^+$) and $PdO_x$,
539 *etc*., in the final Pd-zeolite products.[20,101] While Pd ions occupy the ion-exchange sites,
540 the others are found to locate in the zeolite cage or on the external surface. Lee *et al.*[33]
541 applied a modified titration method to prove that ionic Pd species, rather than bulk PdO,
542 are the main active sites for NO storage on Pd-zeolites at low temperatures. The states
543 of Pd species, in turn, could be affected by NO adsorption. As shown in **Figure 4**b, Pd–
544 O shell, existing predominantly in the oxidized sample, decreased in intensity by more
545 than half after NO exposure at low temperatures.[54] The shift of edge energy to the range
546 between metallic Pd and PdO in **Figure 4**a implies that a majority of Pd species is
547 monovalent in NO-adsorbed Pd-zeolite, consistent with the reduction of $Pd^{II}$ to $Pd^I$.[54]
548 Relevant mechanism are presented in more detail in Section 3.2.

549 Reversable transformation between $Pd^0$ (or $PdO_x$) and isolated $Pd^{2+}$ can occur by
550 specific treatments.[42,83,89] For example, sequential $H_2$/CO reduction and NO treatment
551 could lead to redispersion and transformation of encaged small PdO nanoparticles into
552 $Pd^{2+}$ inside zeolite framework.[41,102] By performing $H_2$ reduction at 500 °C and
553 subsequent NO exposure at 600 °C over the conventionally synthesized Pd-CHA,
554 Yasumura *et al.*[42] achieved atomic dispersion of bulk Pd on the external surface to Pd
555 cations inside zeolites. Thereby, the authors obtained a Pd-CHA zeolite catalyst with a
556 relatively high loading (4.1 wt.%) of atomically dispersed $Pd^{2+}$ at the exchange sites on
557 CHA framework. **Figure 7**a intuitively displays the remarkable change in Pd dispersion
558 after the two-step treatment. The O atom by NO dissociation reacts with a surface Pd
559 atom of bulk Pd to form a mononuclear PdO,[103] which can easily diffuse and further
560 react with zeolite protons to form isolated $Pd^{2+}$ anchored by an ion-exchange site at the
561 6MR (Eq. 2). Note that the process of PdO formation needs a high temperature, and
562 only in the feed containing $NO_x$ can Eq. 2 occur.

$$PdO + 2\,Z^{-}H^{+} \rightarrow Z_2^{-}Pd^{2+} + H_2O \quad (2)$$

The NO-facilitated transformation of $Pd^0$ to $Pd^{2+}$ is demonstrated in Eq. 3.[102]

$$Pd^0 + 2\,NO + 2\,Z^{-}H^{+} \rightarrow Z_2^{-}Pd^{2+} + N_2O + H_2O \quad (3)$$

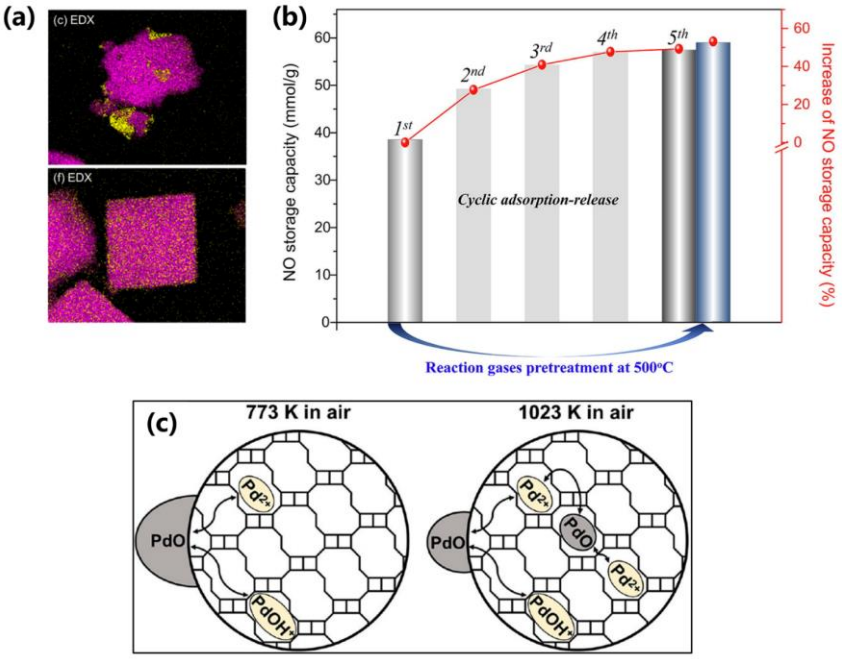


**Figure 7.** (a) EDX mapping (Pd-yellow, Si-purple) for Pd-CHA before (top) and after (bottom) sequential $H_2$ reduction/NO exposure treatments. Reproduced with permission from ref 42. Copyright 2021 Yasumura *et al.* (b) NO adsorption capacity on Pd-ZSM-11 after different NO adsorption–release cycles ($1^{st}$–$5^{th}$) and after the pretreatment at 500 °C with 200 ppm NO and 10 vol.% $O_2/N_2$ for 2 h. Reproduced with permission from ref 83. Copyright 2020 Elsevier. (c) An evolution diagram of Pd species on/in CHA when oxidized at different temperatures in air. Reproduced with permission from ref 89. Copyright 2021 American Chemical Society.

Similarly, a direct NO+$O_2$ pretreatment at 500 °C also led to more ionic Pd sites in Pd-zeolites and thus increased $NO_x$ storage capacity, as demonstrated in **Figure 7**b for Pd-ZSM-11.[83] *In situ* CO-DRIFTS study confirmed a higher density of Pd ions in the Pd-zeolite sample treated with NO+$O_2$ than that treated with $O_2$ only, suggesting a redistribution of agglomerated Pd to highly dispersed Pd species.[83] Usually, treatments with strong oxidants such as $O_2$ are believed to induce PdO agglomeration at zeolite surface, and are thus detrimental to the generation of $Pd^{2+}$ at moderate or high temperatures.[104] However, Lardinois *et al.* found that high-temperature (750 °C)

treatment in air could provide driving force for the disruption and diffusion of agglomerated PdO into the pores and channels of CHA, and then forming isolated $Pd^{2+}$ ions (**Figure 7**c).[89]

### 3.2 $NO_x$ adsorption/desorption mechanism

According to studies combined EXAFS/XANES, X-ray photoelectron spectroscopy and theoretical simulation, isolated $Pd^{2+}$ ions are the most stable primary adsorption sites during NO exposure, whereas $[Pd(OH)]^+$ sites and $PdO_2$ clusters can be reduced by NO to $Pd^+$ ions and monomeric PdO, respectively, for further NO adsorption.[20,54,63] Detailed NO adsorption processes on different Pd sites are listed as follows.

$$Z_2^-Pd^{2+} + NO \rightarrow Z_2^-Pd^{2+}\text{–}NO \quad (4)$$

$$2\,Z^-[Pd(OH)]^+ + 3\,NO \rightarrow 2\,Z^-Pd^+\text{–}NO + NO_2 + H_2O \quad (5)$$

$$PdO_2 + 2\,NO \rightarrow (NO)PdO + NO_2 \quad (6)$$

Apart from Pd species, the spare BASs of zeolites also contribute to the storage capacity by adsorbing NO as $NO^+$, which easily desorbs at 100–200 °C.[105–107] It has to be noted that the above-mentioned NO storage processes occur in the absence of $H_2O$. With $H_2O$ vapor in the feed gas, NO adsorption on reducible Pd species (Eqs. 5 and 6) and BASs will be significantly restrained.[20,43] On account of the renewability of PNA, Pd sites need to be recovered after NO desorption. Further DFT calculations[84,108] confirmed the presence of NO desorption processes that reverse to the above adsorption reactions, as displayed below in Eqs. 7–9.

$$Z_2^-Pd^{2+}\text{–}NO \rightarrow Z_2^-Pd^{2+} + NO \quad (7)$$

$$2\,Z^-Pd^+\text{–}NO + H_2O + 1/2\,O_2 \rightarrow 2\,Z^-[Pd(OH)]^+ + 2\,NO \quad (8)$$

$$(NO)PdO + 1/2\,O_2 \rightarrow PdO_2 + NO \quad (9)$$

In a typical $NO_x$ storage/release profile, a prominent storage peak appears

607 immediately at the switch from bypass to the catalyst, whereas another weak storage
608 peak appears between 100 °C and 200 °C under $H_2O$ (**Figure 2**d).[30,43] During the $NO_x$
609 release stage, two distinguishable desorption peaks are normally observed in a low-
610 temperature range (150–250 °C) and a high-temperature (250–400 °C) range, which
611 can be assigned to $Pd^{2+}$ and $Pd^{+}$, respectively, according to a stronger bond strength of
612 $Pd^{2+}$–NO than $Pd^{+}$–NO.[84,108] Detailed $NO_x$ adsorption/desorption mechanism under
613 feed gas containing different components will be elaborated in Section 3.3.

614 **3.3 Interactions between Pd sites and exhaust components**

615 *3.3.1 $H_2O$*

616 Engine exhausts inevitably include $H_2O$ originating from fuel combustion or
617 moisture in air. The presence of $H_2O$ has a well-known adverse influence on the PNA
618 function of Pd-zeolites.[108–110] As indicated in **Figure 8**a, when $H_2O$ was added to the
619 gas feed, the $NO_x$ adsorption capacity of Pd-SSZ-13 suffered a drastic loss and a second
620 stage of $NO_x$ storage occurred at ~200 °C. Meanwhile, $NO_x$ desorption temperature was
621 considerably elevated.[43] Similar results have been reported in several other
622 works.[20,57,108] From *in situ* NO-DRIFTS (**Figure 8**b), one can easily observe that the
623 bands at 2200–2100 $cm^{-1}$ for $NO^{+}$ on BASs of Pd-zeolite disappeared during exposure
624 in feed gas containing $H_2O$, which is due to the occupation of BASs by $H_2O$ (as shown
625 by the band at 1700–1600 $cm^{-1}$ for molecularly adsorbed $H_2O$ on BASs[106]) restricting
626 NO adsorption.[24,111] In addition, the bands at 1900–1800 $cm^{-1}$ for NO adsorption as
627 nitrosyl complexes on ionic Pd species were observed to form a main band with a weak
628 shoulder in the presence of $H_2O$.[65,82,112]

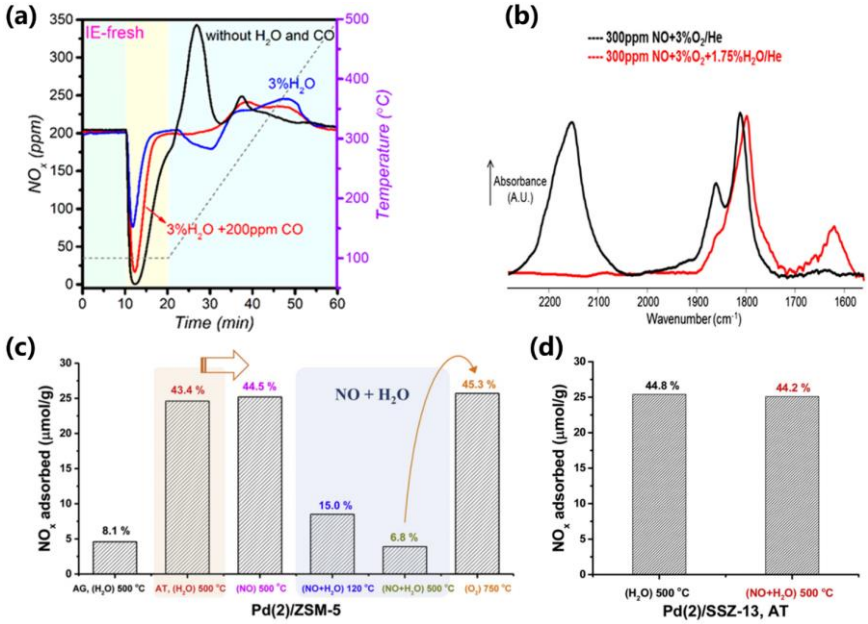


**Figure 8.** (a) $NO_x$ profiles of freshly calcined Pd-SSZ-13 synthesized with an IE method. Gas feed: 3 vol.% $H_2O$ (if added), 200 ppm $NO_x$, 200 ppm CO (if added) and 10 vol.% $O_2/N_2$. Reproduced with permission from ref 43. Copyright 2021 American Chemical Society. (b) NO-DRIFTS spectra collected at 100 °C for Pd-SSZ-13 after exposure to NO+$O_2$ with or without $H_2O$ in the gas mixtures. Reproduced with permission from ref 24. Copyright 2016 Springer Nature. NO adsorption capacities of (c) Pd(2)/ZSM-5 and (d) Pd(2)/SSZ-13 after various treatments with NO or/and $H_2O$. Reproduced with permission from ref 109. Copyright 2020 Elsevier.

It was repeatedly suggested that $H_2O$ limits the NO adsorption on Pd species by inducing hydrolysis or hydration of Pd ions (primarily $[Pd(OH)]^+$) to form $[Pd(OH)_4]^{2-}$, $[Pd(OH)_3(H_2O)]^-$, $[Pd(OH)_2(H_2O)_2]$ or $[Pd(H_2O)_n]^{2+}$.[57,65,82] As displayed in **Figure 4**d, the $Pd(H_2O)_4^{2+}$ complex at 410 $nm^{-1}$, which was observed in the UV-Vis spectra of hydrated Pd-zeolites, disappeared after dehydration, leading to bare $Pd^{2+}$ (*i.e.*, the band at 450 $nm^{-1}$) at the exchange sites in the zeolite.[57] According to the least ionic Pd sites and the largest drop of $NO_x$/Pd ratio on Pd-SSZ-13 among various Pd-zeolites, Zheng *et al.* proposed that $H_2O$ would inhibit the reaction between NO and $PdO_x$ clusters, instead of Pd ions, and eventually deactivate the Pd-zeolites.[20] The temporary inhibition of NO adsorption generally disappears along with $H_2O$ desorption at temperatures above 100 °C, explaining the second NO adsorption peak in typical PNA profiles

649 (**Figure 8**a).[20,65]

650 The $H_2O$ effect on Pd-zeolites aggravates with the increasing pore size of
651 zeolites.[109] Lee *et al.* compared the NO adsorption capacities of Pd-ZSM-5 and Pd-
652 SSZ-13 with the same Pd loading of 2 wt.% (denoted as Pd(2)/ZSM-5 and Pd(2)/SSZ-
653 13, respectively) after pretreatment in $H_2O$ and NO.[109] The amount of adsorbed NO,
654 while decreased severely on Pd(2)/ZSM-5, remained nearly constant on Pd(2)/SSZ-13
655 after treatment in NO+$H_2O$ mixtures at 500 °C (**Figure 8**c and **8**d). On the contrary,
656 there was almost no difference in the NO storage ability of the two Pd-zeolites after
657 pretreatment in NO or $H_2O$ alone, pointing to a better resistance of Pd(2)/SSZ-13 to
658 NO/$H_2O$ co-adsorption. It was suggested that $Pd^{2+}(H_2O)(NO)$ would be formed during
659 NO adsorption in the presence of $H_2O$, rendering higher mobility of Pd species and
660 accelerating PdO agglomeration.[109,113] A better resistance of Pd-SSZ-13 than Pd-ZSM-
661 5 to environment can be attributed to the lower Pd mobility in SSZ-13 with a smaller
662 pore size,[25,36] which is more suitable for practical PNA applications.

663 *3.3.2 CO*

664 CO-induced deactivation of Pd-zeolites has been reported frequently in literatures.
665 Gu *et al.*[46] found that the presence of CO in gas feed led to a slightly reduced $NO_x$
666 adsorption capacity of Pd-zeolites in cyclic PNA tests, as displayed by the $NO_x$/Pd ratios
667 in the brackets behind every legend in **Figure 9**a. For Pd-BEA-750HTA, an irreversible
668 deactivation was noted after two cycles of NO/CO co-adsorption (namely "After CO
669 Exposure"), as indicated by a lower capacity in the third cycle of NO adsorption without
670 CO. Analogous deactivation was indicated on Pd-SSZ-13 after multiple PNA cycles
671 under a simulated exhaust gas from low-temperature diesel combustion (*i.e.*, 2000 ppm
672 CO, 100 ppm NO, 6 vol.% $H_2O$, 6 vol.% $CO_2$ and 12 vol.% $O_2$).[114] Furthermore, a
673 degradation of Pd-SSZ-13 induced by reducing gas (CO or $H_2$) at high temperatures,

674 intensifying with the increase of reduction treatment temperature, was found by Ryou
675 *et al.*[81] Based on $H_2$-TPR results (**Figure 9**b), a complete reduction of $Pd^{2+}$ was
676 observed on Pd-BEA after CO exposure at 80 °C and a subsequent TPD to 200 °C.[46]
677 Combining the STEM evidence showing the appearance of large Pd particles in the
678 sample after CO exposure,[46,81] one could conclude that, due to the complete reduction
679 of $Pd^{2+}$ and the particle aggregation, CO exposure at temperatures below 200 °C would
680 cause an irreversible loss of $Pd^{2+}$ and, in turn, a reduction of $NO_x$ storage capability.

681 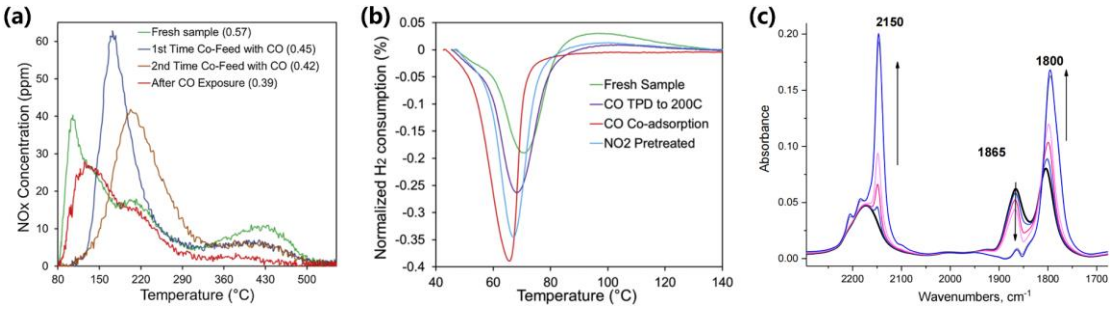


682 **Figure 9.** (a) $NO_x$-TPD profiles of Pd-BEA-750HTA after consecutive $NO_x$ storage cycles. The
683 storage tests of "Fresh sample" and "After CO Exposure" were performed in 200 ppm NO, 5
684 vol.% $H_2O$ and 10 vol.% $O_2$, while 200 ppm CO was added into the feed during storage tests
685 of "1st/2nd Time Co-Feed with CO". (b) $H_2$-TPR profiles of the Pd-BEA-750HTA sample in
686 fresh state, after CO exposure at 80 °C followed by a TPD to 200 °C, after three cycles of
687 NO/CO co-adsorption and TPD, and after treatment by $NO_2$. Reproduced with permission from
688 ref 46. Copyright 2019 Elsevier. (c) FTIR spectra collected during step-wise addition of CO to
689 a NO-saturated Pd-SSZ-13. Reproduced with permission from ref 65. Copyright 2018
690 American Chemical Society.

691 Interestingly, CO also demonstrates unexpected beneficial effects in PNA at low
692 temperatures (~100 °C). The presence of CO in the reaction mixture promoted
693 significantly $NO_x$ adsorption on Pd-SSZ-13 under $H_2O$, and eliminated the second $NO_x$
694 uptake at *ca.* 200 °C (**Figure 8**a).[30,43] The change in $NO_x$ storage/release induced by CO
695 was supposed to be associated with the formation of $Pd^{2+}$(NO)(CO) species.[30,65,87] As
696 shown in **Figure 9**c, exposure of NO-saturated Pd-SSZ-13 to CO led to a decrease of
697 band intensity at 1865 $cm^{-1}$ for the $\nu$(NO) vibrations of $Pd^{2+}$–NO species, and an

698 increase of band intensities at 2150 $cm^{-1}$ for $\nu$(CO) vibrations and at 1800 $cm^{-1}$ for
699 $\nu$(NO) vibrations, corresponding to a selective conversion of $Pd^{2+}$–NO species into a
700 stable mixed carbonyl–nitrosyl complex, *i.e.*, $Pd^{2+}$(NO)(CO), as evidenced by DFT
701 calculations.[30,65] This process of selective transformation is summarized in Eq. 10,
702 based on a stronger binding energy of $Pd^{2+}$–NO than that of $Pd^{2+}$–CO as proved by
703 subsequent vacuum desorption studies.[65] The coordinatively saturated and stable
704 $Pd^{2+}$(NO)(CO) complex prevents $H_2O$ from coordinating with $Pd^{2+}$ sites, rendering Pd-
705 SSZ-13 relatively high $NO_x$ adsorption capacity in the presence of $H_2O$.[30,65] The
706 restoration of $NO_x$ storage capacity, which increased with the CO concentration in feed
707 gas,[115] was manifested to be more significant on Pd-SSZ-13 than on Pd-Beta or Pd-
708 ZSM-5.[20] The $NO_x$ release temperature also increased in the presence of CO, because
709 CO needs to be released first from the complex.[65]

710 $$Pd^{2+}\text{–NO} + \text{CO} \rightarrow Pd^{2+}(\text{NO})(\text{CO}) \quad (10)$$

711 Besides, low-temperature CO may change the $NO_x$ storage/release properties of
712 Pd-zeolites by partially reducing Pd species. In the DRIFT spectra with CO feeding, the
713 new features with lower wavenumbers were ascribed to a more stable species formed
714 by NO binding with the Pd ions of a lower oxidation state (due to reduction by CO),
715 heightening $NO_x$ storage ability and increasing $NO_x$ release temperature.[115] Yao *et al.*
716 developed a multi-site kinetic model to simulate the CO-assisted pathways of $NO_x$
717 storage/release on Pd-SSZ-13 by incorporating the reactions of diverse Pd sites with
718 CO.[44] It could be deduced that, after adding CO, nearly all the Pd species were
719 converted to Pd sites that interact more strongly with $NO_x$. The reduction process of
720 ionic Pd species (*i.e.*, $Z^-[Pd(OH)]^+$) by CO is illustrated in Eq. 11.

721 $$2\ Z^-[Pd(OH)]^+ + 2\ \text{NO} + \text{CO} \rightarrow 2\ Z^-Pd^+\text{–NO} + CO_2 + H_2O \quad (11)$$

722 In summary, when a fresh PNA catalyst is put into operation, CO in the low-

723 temperature exhaust enhances $NO_x$ storage by mitigating the shielding effect of $H_2O$ in
724 the following ways: (1) forming a stable $Pd^{2+}(NO)(CO)$ complex; (2) reducing
725 $[Pd(OH)]^+$ to $Pd^+$ which has a stronger interaction with $NO_x$. However, CO exposure
726 above adsorption temperatures may lead to the reduction of $Pd^{II}$ to $Pd^0$ and thus the
727 deactivation of Pd-zeolites.

728 *3.3.3 HCs*

729 Various HCs, such as small-molecule olefins and long-chain alkanes, also exist in
730 diesel exhausts at times. Although there are already attempts to explore the potential of
731 zeolites as passive HC adsorbers,[86,116] the influence of HCs on PNA using Pd-zeolites
732 is yet to be expounded. Predictions by a transient monolith model predicted that more
733 NO molecules were adsorbed by Pd-zeolites in PNA with the presence of CO or $C_2H_4$
734 in the gas feed, and $C_2H_4$ was less effective than CO in promoting NO adsorption
735 (**Figure 10**a).[46] Liu *et al.*[117] found that the introduction of $C_3H_6$ increased the $NO_x$
736 storage capacity of Pd-zeolites and delayed the NO desorption to higher temperatures
737 (**Figure 10**b). In the *in situ* FTIR spectra shown in **Figure 10**c, the characteristic band
738 at 1807 $cm^{-1}$ for $Pd^+$–NO increased further in intensity from 1024 to 1207 s, which can
739 be attributed to the NO re-adsorption on $Pd^+$ generated after adding $C_3H_6$.[117] From 1207
740 to 1679 s, the 1746 $cm^{-1}$ band, assigned to $Pd^+$–$NC_3H_6O$, increased at the expense of
741 the 1807 $cm^{-1}$ band. The possible reaction steps are listed below.

742 $$2\,Z^-[Pd(OH)]^+ + 2\,NO + C_3H_6 \rightarrow 2\,Z^-Pd^+\text{–}NO + C_3H_6O + H_2O \quad (12)$$

743 $$Pd^+\text{–}NO + C_3H_6 \rightarrow Pd^+\text{–}NC_3H_6O \quad (13)$$

744 Eq. 12 elucidates that $C_3H_6$ reduces $[Pd(OH)]^+$ similar as NO and CO. During
745 desorption stage, a reverse reaction with the release of NO from Pd ions occurred (Eq.
746 13). As a result, NO desorption from Pd-zeolites was delayed to higher temperatures
747 due to the formation of intermediate.[117]

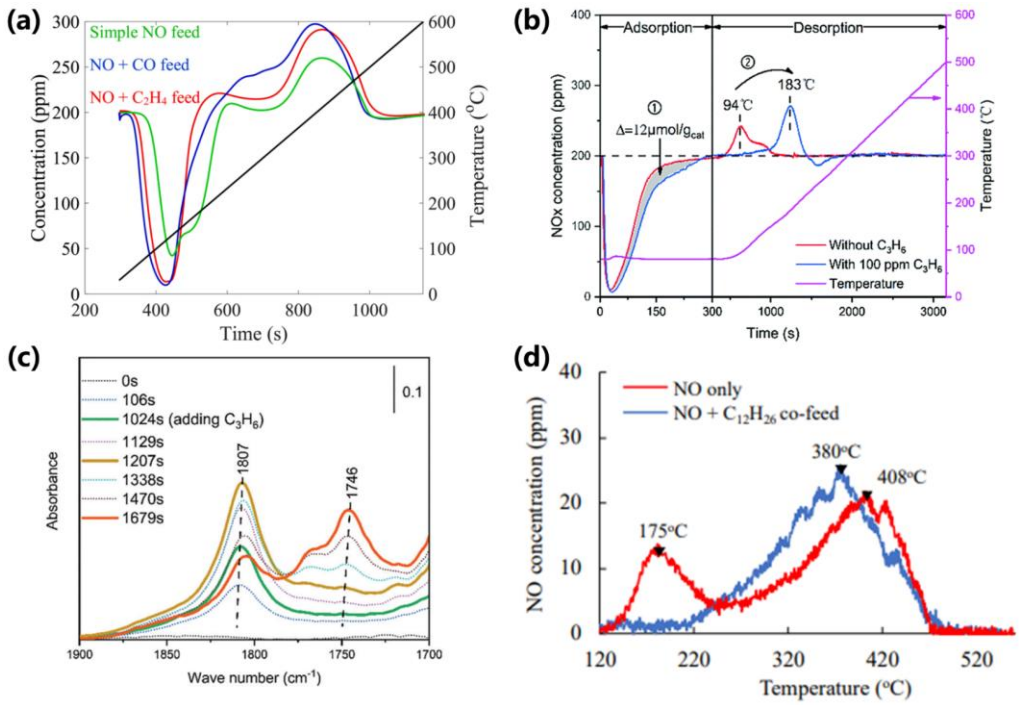


**Figure 10.** (a) Model prediction of NO profiles for simple NO feed, NO+CO feed and NO+$C_2H_4$ feed. Simple NO feed consisted of 200 ppm NO, 12 vol.% $O_2$, 6 vol.% $CO_2$, 6 vol.% $H_2O$ and balance $N_2$. For other feeds, 500 ppm CO or 200 ppm $C_2H_4$ was added to the simple NO feed (without $CO_2$). Reproduced with permission from ref 46. Copyright 2021 Elsevier. (b) $NO_x$ profiles of Pd-Beta under a feed of 200 ppm $NO_x$, 100 ppm $C_3H_6$ (if added), 5 vol.% $H_2O$, and 10 vol.% $O_2/N_2$. (c) FTIR spectra of Pd-Beta at 80 °C when $C_3H_6$ was added into the feed after adsorption saturation in a feed excluding $C_3H_6$. Reproduced with permission from ref 117. Copyright 2021 Elsevier. (d) NO-TPD profiles for NO only feed and NO/$C_{12}H_{26}$ co-feed at ~115 °C. Reproduced with permission from ref 118. Copyright 2021 Elsevier.

On the contrary, long-chain HC molecules, such as $C_{12}H_{26}$, showed almost no effect on the NO adsorption, but prohibited the low-temperature NO release, over Pd-SSZ-13 (**Figure 10**d).[118] However, Pd-SSZ-13 pre-saturated with $C_{12}H_{26}$ suffered a partial loss of NO adsorption capacity. Based on non-bonding interaction between adsorbed molecules and zeolites,[119,120] it was inferred that $C_{12}H_{26}$, which was adsorbed on the zeolite sites through van der Waals interaction, would not compete with NO for the cationic Pd sites. Nonetheless, the pre-adsorbed $C_{12}H_{26}$ molecules, even though located at the external surface, hindered NO from accessing Pd ions within zeolite framework.[118]

767 **3.4 Chemical poisoning**

768 When using lubricant oil additives or impure fuels during practical automotive
769 operation, after-treatment catalysts encounter continuously chemical poisons
770 (phosphorus, sulfur, alkali metals, and so on) in exhausts, and may be deactivated
771 gradually as a result of chemical poisoning which causes the migration and aggregation
772 of active phase, as well as the formation of inert bulk species.[121–124] Chen *et al.*
773 investigated the degradation of Pd-SSZ-13 PNA catalyst by phosphorus (P) poisoning
774 using *in situ* DRIFTS (NO, CO and $NH_3$ as probe molecules), and revealed that
775 $[Pd(OH)]^+$ species located in 8MRs ($[Pd(OH)]^+$@8MR) were more susceptible to P
776 poisoning than $Pd^{2+}$ species in 6MRs ($Pd^{2+}$@6MR).[43] *In situ* CO-DRIFT spectra in
777 **Figure 11**a disclosed that, P poisoning resulted in declined band intensities for
778 $Pd^{2+}$@6MR and $[Pd(OH)]^+$@8MR, and increased band intensities for surface
779 $[Pd(OH)]^+$ species and $Pd^0$ (generated from the reduction of small PdO).[43] Taking these
780 *in situ* DRIFTS observations into account, two kinds of P-poisoning mechanisms were
781 put forward for Pd-SSZ-13 (**Figure 11**b), namely the direct migration of
782 $[Pd(OH)]^+$@8MR from ion-exchange sites to external zeolite surface, and the
783 transformation of $Pd^{2+}$@6MR to $[Pd(OH)]^+$ which then migrated to the zeolitic surface.
784 Ultimately, surface $[Pd(OH)]^+$ species were partially oxidized and agglomerated into
785 bulk $PdO_x$ at high temperatures.[43]

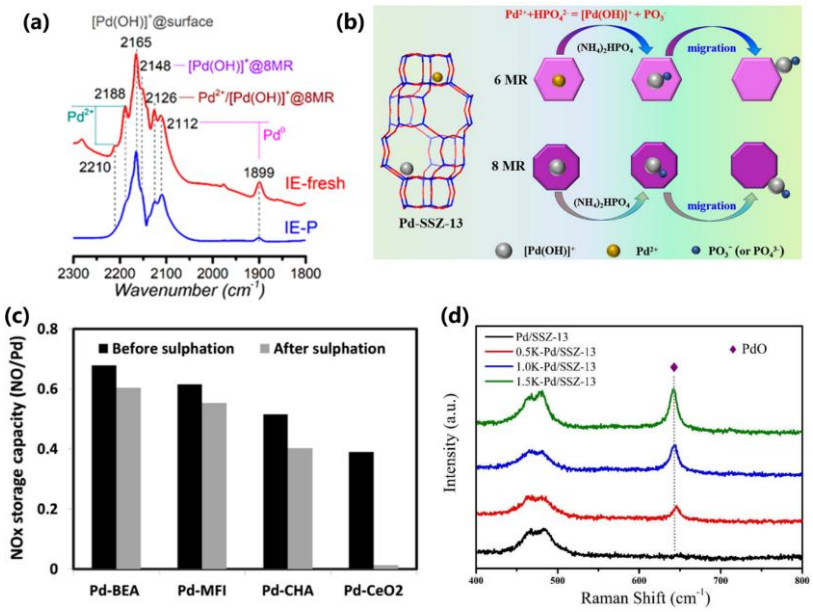


**Figure 11.** (a) Comparison of the *in situ* CO-DRIFT spectra of freshly calcined and P-poisoned Pd-SSZ-13 after CO saturation. (b) Deactivation mechanisms for $Pd^{2+}$ and $[Pd(OH)]^{+}$ sites in Pd-SSZ-13 by P-poisoning. Reproduced with permission from ref 43. Copyright 2021 American Chemical Society. (c) Effect of sulphation on the NO storage capacity at 100 °C for different Pd catalysts with 1 wt.% Pd. Reproduced with permission from ref 24. Copyright 2016 Springer Nature. (d) Raman spectra of the Pd-SSZ-13 and K-deactivated samples. Reproduced with permission from ref 125. Copyright 2016 Fan *et al.*

Zeolites as catalyst supports are popular for its superiority in sulfur tolerance compared with common oxides such as $CeO_2$.[24,126] As shown in **Figure 11**c, while Pd-$CeO_2$ was deteriorated almost completely, the $NO_x$ storage capacities of three Pd-zeolites with different framework types were largely maintained.[24] Mesilov *et al.* predicted, based on DFT simulations, that $SO_2$ poisoned Pd-SSZ-13 mainly through affecting $[Pd(OH)]^{+}$ and PdO clusters, instead of $Pd^{2+}$, by forming Pd bisulfates.[127] A recent study on potassium (K) poisoning (simulated by K impregnation) of Pd-SSZ-13 PNA catalyst revealed that, while the zeolite framework structure kept almost intact, sintering of Pd phase occurred within the pores/channels and on the zeolite surface.[125] The increased amount of PdO in Pd-SSZ-13 with K loading, as shown in **Figure 11**d, suggested that migration and transformation of Pd species played an important part in the K-promoted sintering process.[125]

806 So far, mechanistic understandings about the chemical poisoning of Pd-zeolites as
807 PNA materials are far from systematic and in-depth, as compared to that for Cu-zeolites
808 as $NH_3$-SCR catalysts. To guide the design of novel Pd-zeolite-based PNA catalysts
809 with high resistance to chemical poisons, more attention should be paid to figure out
810 relevant issues like the dynamic changes of active Pd sites in the presence of poisons.

811 **4 PNA integration into exhaust after-treatment systems**

812 PNA is expected to play its role in combination with the SCR unit in a real-world
813 vehicle exhaust purification system. Therefore, single-monolith catalysts with both
814 PNA and SCR coatings or serial PNA+SCR units have been designed for $NO_x$
815 abatement especially at low temperatures (**Figure 12**a and **12**b).[26,128] While the former
816 configurations avert the complexity and expense of additional unit in the whole after-
817 treatment system, the latter configurations could prevent any potential mutual
818 interference by separating the PNA catalyst from the SCR catalyst.[128,129]

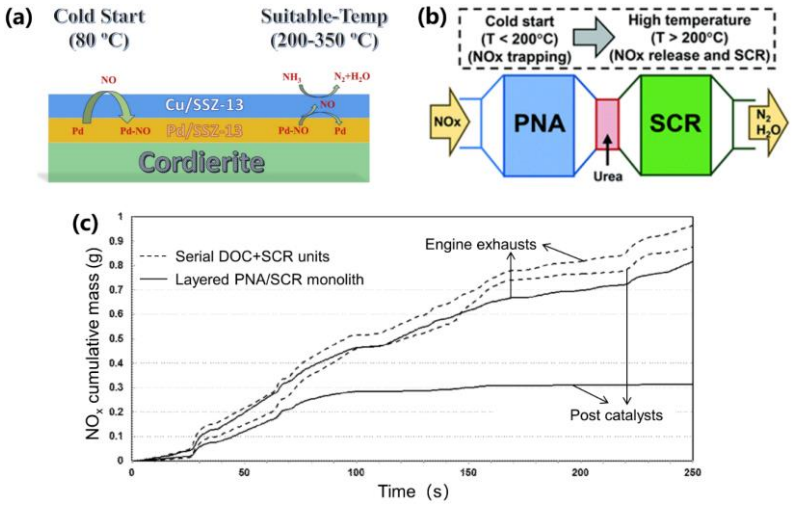

819

820 **Figure 12.** (a) A layered Pd-SSZ-13 with Cu-SSZ-13overlayer as PNA/SCR dual-layer
821 monolith catalyst. Reproduced with permission from ref 128. Copyright 2020 Elsevier. (b)
822 Serial PNA+SCR units in a modern diesel after-treatment system for cold-start $NO_x$ abatement.
823 Reproduced with permission from ref 26. Copyright 2018 The Royal Society of Chemistry. (c)
824 $NO_x$ cumulative mass measured after being released from an engine without after-treatments
825 (*i.e.*, engine exhausts), and after passing through after-treatment catalysts (*i.e.*, post catalysts;
826 catalysts refer to serial DOC+SCR units or a layered PNA/SCR monolith) without urea dosing

827 in the first 250 s of a MVEG (Motor Vehicle Emissions Group) test.[130] DOC refers to diesel
828 oxidation catalyst.

829 Wang *et al.* have devised a dual-layer monolithic catalyst by layered coating,
830 integrating Pd-SSZ-13 as the PNA material and Cu-SSZ-13 as the SCR catalyst.[128] As
831 depicted in **Figure 12**a, $NO_x$ in exhausts are expected to be stored on the bottom Pd-
832 SSZ-13 layer at low temperatures. When reaching a high temperature (> 200 °C) where
833 urea ($NH_3$ source) decomposes and SCR catalysts work effectively, the adsorbed $NO_x$
834 will be released and flow into the upper Cu-SSZ-13 layer, and then be removed through
835 $NH_3$-SCR reactions. Under simulated automotive exhaust conditions, the PNA/SCR
836 monolith showed a decent $NO_x$ trap capacity of 0.73 ($NO_x$/Pd). In addition, $NH_3$-SCR
837 and $NO_x$ desorption tests displayed that the layered monolith catalyst exhibited similar
838 activity as a pure Cu-SSZ-13 below 350 °C, and over 80% of the adsorbed $NO_x$ was
839 released within the temperature range of $NO_x$ conversion above 80%.[128] Granted that
840 this integrated PNA/SCR configuration eliminates a necessity to substantially modify
841 the after-treatment system, $NO_x$ storage capacity of Pd-SSZ-13 was affected
842 unfavorably by two factors, namely over-reduction of partial $Pd^{2+}$ ions by the reductive
843 $NH_3$ in gaseous feeds and disturbance of the Pd species by the coating process of an
844 upper Cu-SSZ-13 layer. In turn, the presence of Pd species brought about non-selective
845 $NH_3$ oxidation above 350 °C and thus a decline in $NO_x$ conversion.[128,131] These issues
846 need to be further investigated and solved, in case practical use prefers this kind of
847 combined device configuration.

848 Burgess *et al.* have applied the concept of a layered PNA/SCR catalyst into engine
849 bench experiments to test the performance discrepancy of exhaust post-treatment
850 device with/without a PNA material.[130] The metal loading and washcoat loading were
851 60 g/ft$^3$ and 1.0 g/in$^3$ for the lower Pd-CHA layer, while those were 120 g/ft$^3$ and 2.4

852 g/in$^3$ for the upper Cu-CHA layer. As depicted in **Figure 12**c, while the serial
853 DOC+SCR units demonstrated little effect on $NO_x$ reduction, the layered PNA/SCR
854 monolith could reduce over 60% of $NO_x$ cumulative mass in the first 250 s (below
855 200 °C). After dosing urea, the layered catalyst could retain constantly a $NO_x$ reduction
856 ability above 50% in the first 1100 s, showing its superiority than commercial
857 DOC+SCR system in cold-start period.[124]

858 Chen *et al.* have devised a novel multifunctional catalytic material comprising Pd
859 and Cu deposited on the same zeolite, which is expected to work effectively as both
860 PNA and SCR catalysts, and even an ammonia slip catalyst (ASC).[132] Compared with
861 the combination of several single catalyst coatings in monolith, such blending of several
862 functions into one catalyst can reduce washcoat loading and back pressure in real
863 applications. A further evaluation in PNA manifested that $NH_3$ addition had no impact
864 on $NO_x$ storage ability of such multifunctional monolith catalyst, and the temperature
865 gap between $NO_x$ release from PNA material and effective operation of SCR catalyst
866 could be removed.[133]

867 The second configuration is the separation of a PNA and an SCR catalyst,
868 including an independent PNA unit or a combined DOC/PNA unit located upstream
869 from the urea dosing unit and the SCR unit (**Figure 12**b).[26,134] For such multi-unit
870 system, most inventors have been devoted to address realistic issues related to the
871 presence of PNA. For example, DOC can be combined to reduce the amount of $N_2O$
872 generated from the reaction of HCs and $NO_x$ adsorbed on PNA,[134] and ozone generator
873 or heating element can be added to improve $NO_x$ conversion on downstream SCR
874 catalyst.[135,136]

875 Frankly, more and more related patents attend to devise layered or zoned monolith
876 catalysts being able to reduce $NO_x$ and to oxidize other contaminants (HCs, CO, $NH_3$,

877 *etc.*) simultaneously, as do basic researches.[137] In this instance, it's quite necessary to
878 strike a balance among purification performance of each catalytic component by
879 optimizing material selection and coating/zoning design.

880 **5 Challenges and implications**

881 Even though substantial progress has already been achieved in this field, there are
882 still important issues to be resolved, both fundamentally and practically. While zeolites
883 with small crystal sizes appear to perform more satisfactorily in a large variety of
884 catalytic reactions, it is puzzling why Pd-BEA with larger crystals surpasses those with
885 nanocrystals in terms of $NO_x$ uptake and hydrothermal stability.[70] Apart from
886 framework defects, the nature of framework T-atoms and the crystal morphology are
887 likely key points for future PNA research as well.[138] The promotional effect of
888 hydrothermal aging on the PNA performance of Pd-zeolites needs to be elucidated
889 mechanistically. $Pd^+$ ions, which are predicted to be the most stable ionic Pd sites for
890 $NO_x$ adsorption by several theoretical models, are not verified experimentally. In
891 consideration of this controversy, electron paramagnetic resonance spectroscopy, which
892 is frequently employed in the study of Cu-exchanged zeolites, may play a role by
893 identifying the valence and local environment of Pd species in Pd-zeolites.[17,97]
894 Response of ionic Pd sites to chemical poisons (P, S, Zn, alkali metals, *etc.*) is also
895 waiting for further investigation. While the simultaneous capture of $NO_x$, CO and/or
896 HCs by Pd-zeolites was noticed during the adsorption stage,[43,61] behaviors and
897 mechanisms of CO/HCs oxidation accompanying $NO_x$ release have not unraveled yet
898 and need to be interrogated systematically for developing novel multifunctional Pd-
899 zeolite catalysts. Furthermore, Pd speciation and transformation during cyclic PNA
900 tests deserve more attention for improving the durability of Pd-zeolites.

901 For real applications, PNA component in a multifunctional monolith catalyst
902 should retain its function against the interference of multiple gaseous pollutants (*e.g.*,
903 CO, HCs, $NH_3$), while minimizing detrimental effects on other purification units, such
904 as the Pd-catalyzed non-selective $NH_3$ oxidation that induces a decreased $NO_x$
905 conversion of the SCR component.[128,131] Irreversible deactivation of Pd-zeolites due to
906 CO-induced Pd reduction, which is widely considered to be a major obstacle for the
907 commercialization of PNA, may be mitigated by reasonably coupling PNA with the
908 DOC catalyst. Regeneration after deposition of S, P, HCs, coke, *etc*., which is critical
909 for exhaust after-treatment applications,[139–141] has been rarely studied on Pd-zeolite
910 PNA catalysts, and needs to be investigated in depth for improving the durability.
911 Frankly speaking, close-coupled SCR catalysts and electric heaters seem to be more
912 realistic solutions for cold-start $NO_x$ emission control at present.[142–145] Nevertheless,
913 with further advances in material development and system optimization, especially the
914 resolution of above-discussed critical issues for Pd-zeolites, integrating PNA into
915 monolith catalyst is still a highly potential all-in-one strategy to meet more stringent
916 future legislations on the cold-start emission of multiple pollutants (including $NO_x$, CO,
917 HCHO, $NH_3$, $CH_4$, *etc.*) from heavy-duty lean-burn vehicles.

918 **Acknowledgments**

919 This work was supported by the National Natural Science Foundation of China
920 (21976058), the Science and Technology Program of Guangzhou (202102080490), the
921 Fundamental Research Funds for the Central Universities (2022ZYGXZR018) and the
922 National Engineering Laboratory for Mobile Source Emission Control Technology
923 (NELMS2020A10). P.C. appreciates the funding from the Pearl River Talent
924 Recruitment Program of Guangdong Province (2019QN01L170) and the Innovation &
925 Entrepreneurship Talent Program of Shaoguan City. We appreciate the fruitful

discussions and helpful suggestions from Dr. Kunpeng Xie (Volvo Group Trucks Technology).

## References

[1] Tan, E.C.D.; Hawkins, T.R.; Lee, U.; Tao, L.; Meyer, P.A.; Wang, M.; Thompson, T. Biofuel options for marine applications: technoeconomic and life-cycle analyses. *Environ. Sci. Technol.* **2021**, *55*, 7561–7570.

[2] Kegl, T.; Kovač Kralj, A.; Kegl, B.; Kegl, M. Nanomaterials as fuel additives in diesel engines: a review of current state, opportunities, and challenges. *Progr. Energy Combust. Sci.* **2021**, *83*, 100897.

[3] Tamilselvan, P.; Nallusamy, N.; Rajkumar, S. A comprehensive review on performance, combustion and emission characteristics of biodiesel fuelled diesel engines. *Renew. Sust. Energ. Rev.* **2017**, *79*, 1134–1159.

[4] Preble, C.V.; Harley, R.A.; Kirchstetter, T.W. Control technology-driven changes to in-use heavy-duty diesel truck emissions of nitrogenous species and related environmental impacts. *Environ. Sci. Technol.* **2019**, *53*, 14568–14576.

[5] Karjalainen, P.; Rönkkö, T.; Simonen, P.; Ntziachristos, L.; Juuti, P.; Timonen, H.; Teinilä, K.; Saarikoski, S.; Saveljeff, H.; Lauren, M.; Happonen, M.; Matilainen, P.; Maunula, T.; Nuottimäki, J.; Keskinen, J. Strategies to diminish the emissions of particles and secondary aerosol formation from diesel engines. *Environ. Sci. Technol.* **2019**, *53*, 10408–10416.

[6] Alam, M.S.; Zeraati-Rezaei, S.; Xu, H.; Harrison, R.M. Characterization of gas and particulate phase organic emissions ($C_9$–$C_{37}$) from a diesel engine and the effect of abatement devices. *Environ. Sci. Technol.* **2019**, *53*, 11345–11352.

[7] Tan, Y.; Yoon, S.; Ruehl, C.R.; Herner, J.; Henderick, P.; Montes, T.; Latt, J.; Lee, A.; Florea, E.; Lemieux, S.; Robertson, W.; Hu, S.; Huai, T. Assessment of in-use $NO_x$ emissions from heavy-duty diesel vehicles equipped with selective catalytic reduction systems. *Environ. Sci. Technol.* **2021**, *55*, 13657–13665.

[8] Tan, Y.; Henderick, P.; Yoon, S.; Herner, J.; Montes, T.; Boriboonsomsin, K.; Johnson, K.; Scora, G.; Sandez, D.; Durbin, T. D. On-board sensor-based $NO_x$ emissions from heavy-duty diesel vehicles. *Environ. Sci. Technol.* **2019**, *53*, 5504–5511.

[9] Grange, S.K.; Farren, N.J.; Vaughan, A.R.; Rose, R.A.; Carslaw, D.C. Strong temperature dependence for light-duty diesel vehicle $NO_x$ emissions. *Environ. Sci. Technol.* **2019**, *53*, 6587–6596.

[10] Krishnamoorthi, M.; Malayalamurthi, R.; He, Z.; Kandasamy, S. A review on low temperature combustion engines: performance, combustion and emission characteristics. *Renew. Sust. Energ. Rev.* **2019**, *116*, 109404.

[11] Kim, B.-S.; Jeong, H.; Bae, J.; Kim, P.S.; Kim, C.H.; Lee, H. Lean $NO_x$ trap catalysts with high low-temperature activity and hydrothermal stability. *Appl. Catal. B* **2020**, *270*, 118871.

[12] Han, L.; Cai, S.; Gao, M.; Hasegawa, J.-y.; Wang, P.; Zhang, J.; Shi, L.; Zhang, D. Selective catalytic reduction of $NO_x$ with $NH_3$ by using novel catalysts: state of the art and future prospects. *Chem. Rev.* **2019**, *119*, 10916–10976.

[13] Wang, J.; Zhao, H.; Haller, G.; Li, Y. Recent advances in the selective catalytic reduction of $NO_x$ with $NH_3$ on Cu-chabazite catalysts. *Appl. Catal. B* **2017**, *202*, 346–354.

[14] Shan, Y.; Du, J.; Zhang, Y.; Shan, W.; Shi, X.; Yu, Y.; Zhang, R.; Meng, X.; Xiao, F.-S.; He, H. Selective catalytic reduction of $NO_x$ with $NH_3$: opportunities and challenges of Cu-based small-pore zeolites. *Natl. Sci. Rev.* **2021**, *8*, nwab010.

[15] Andana, T.; Rappé, K.G.; Gao, F.; Szanyi, J.; Pereira-Hernandez, X.; Wang, Y. Recent advances in hybrid metal oxide-zeolite catalysts for low-temperature selective catalytic reduction of $NO_x$ by ammonia. *Appl. Catal. B* **2021**, *291*, 120054.

[16] Timothy, V.; Johnson. Vehicular emissions in review. *SAE Int. J. Engines* **2012**, *5*, 216–234.

[17] Beale, A.M.; Gao, F.; Lezcano-Gonzalez, I.; Peden, C.H.F.; Szanyi, J. Recent advances in automotive catalysis for $NO_x$ emission control by small-pore microporous materials. *Chem. Soc. Rev.* **2015**, *44*, 7371–7405.

[18] Chen, H.-Y.; Mulla, S.; Weigert, E.; Camm, K.; Ballinger, T.; Cox, J.; Blakeman, P. Cold start concept (CSC™): a novel catalyst for cold start emission control. *SAE Int. J. Fuels Lubr.* **2013**, 372–381.

[19] Cole, J. A. System for reducing $NO_x$ from mobile source engine exhaust. US 5656244 A, 1997.

[20] Zheng, Y.; Kovarik, L.; Engelhard, M.H.; Wang, Y.; Wang, Y.; Gao, F.; Szanyi, J. Low-temperature Pd/zeolite passive $NO_x$ adsorbers: structure, performance, and adsorption chemistry. *J. Phys. Chem. C* **2017**, *121*, 15793–15803.

[21] Ji, Y.Y.; Bai, S.L.; Crocker, M. $Al_2O_3$-based passive $NO_x$ adsorbers for low temperature applications. *Appl. Catal. B* **2015**, *170*, 283–292.

[22] Theis J. R.; Lambert, C. K. An assessment of low temperature $NO_x$ adsorbers for cold-start $NO_x$ control on diesel engines, *Catal. Today* **2015**, *258*, 367–377.

[23] Theis, J.R. An assessment of Pt and Pd model catalysts for low temperature $NO_x$ adsorption. *Catal. Today* **2016**, *267*, 93–109.

[24] Chen, H.Y.; Collier, J.E.; Liu, D.X.; Mantarosie, L.; Duran-Martin, D.; Novak, V.; Rajaram, R.R.; Thompsett, D. Low temperature NO storage of zeolite supported Pd for low temperature diesel engine emission control. *Catal. Lett.* **2016**, *146*, 1706–1711.

[25] Lee, J.; Ryou, Y.; Hwang, S.; Kim, Y.; Cho, S. J.; Lee, H.; Kim, C. H.; Kim, D.H. Comparative study of the mobility of Pd species in SSZ-13 and ZSM-5, and its implication for their activity as passive $NO_x$ adsorbers (PNAs) after hydro-thermal aging. *Catal. Sci. Technol.* **2019**, *9*, 163–173.

[26] Moliner, M.; Corma, A. From metal-supported oxides to well-defined metal site zeolites: the next generation of passive $NO_x$ adsorbers for low-temperature control of emissions from diesel engines. *React. Chem. Eng.* **2019**, *4*, 223–234.

[27] Gu, J.; Zhang, Z.; Hu, P.; Ding, L.; Xue, N.; Peng, L.; Guo, X.; Lin, M.; Ding, W. Platinum nanoparticles encapsulated in MFI zeolite crystals by a two-step dry gel conversion method as a highly selective hydrogenation catalyst. *ACS Catal.* **2015**, *5*, 6893–6901.

1008 [28] Rivallan, M.; Seguin, E.; Thomas, S.; Lepage, M.; Takagi, N.; Hirata, H.; Thibault-Starzyk,
1009 F. Platinum sintering on H-ZSM-5 followed by chemometrics of CO adsorption and 2D
1010 pressure-jump IR spectroscopy of adsorbed species. *Angew. Chem. Int. Ed.* **2010**, *49*, 785–
1011 789.
1012 [29] Moliner, M.; Gabay, J. E.; Kliewer, C.E.; Carr, R. T.; Guzman, J.; Casty, G. L.; Serna, P.;
1013 Corma, A. Reversible transformation of Pt nanoparticles into single atoms inside high-
1014 silica chabazite zeolite. *J. Am. Chem. Soc.* **2016**, *138*, 15743–15750.
1015 [30] Khivantsev, K.; Jaegers, N.R.; Kovarik, L.; Hanson, J.C.; Tao, F.F.; Tang, Y.; Zhang, X.;
1016 Koleva, I.Z.; Aleksandrov, H.A.; Vayssilov, G.N.; Wang, Y.; Gao, F.; Szanyi, J. Achieving
1017 atomic dispersion of highly loaded transition metals in small-pore zeolite SSZ-13: high-
1018 capacity and high-efficiency low-temperature CO and passive $NO_x$ adsorbers. *Angew.*
1019 *Chem. Int. Ed.* **2018**, *57*, 16672–16677.
1020 [31] Aleksandrov, HA.; Neyman, K.M.; Hadjiivanov, K.I.; Vayssilov, G.N. Can the state of
1021 platinum species be unambiguously determined by the stretching frequency of an adsorbed
1022 CO probe molecule? *Phys. Chem. Chem. Phys.* **2016**, *18*, 22108–22121.
1023 [32] Ryou, Y.; Lee, J.; Cho, S.J.; Lee, H.; Kim, C.H.; Kim, D.H. Activation of Pd/SSZ-13
1024 catalyst by hydrothermal aging treatment in passive NO adsorption performance at low
1025 temperature for cold start application. *Appl. Catal. B* **2017**, *212*, 140–149.
1026 [33] Lee, J.; Ryou, Y.; Cho, S.J.; Lee, H.; Kim, C.H.; Kim, D.H. Investigation of the active sites
1027 and optimum Pd/Al of Pd/ZSM–5 passive NO adsorbers for the cold-start application:
1028 evidence of isolated-Pd species obtained after a high-temperature thermal treatment. *Appl.*
1029 *Catal. B* **2018**, *226*, 71–82.
1030 [34] Wang, A.; Lindgren, K.; Di, M.; Bernin, D.; Carlsson, P.-A.; Thuvander, M.; Olsson, L.
1031 Insight into hydrothermal aging effect on Pd sites over Pd/LTA and Pd/SSZ-13 as PNA
1032 and CO oxidation monolith catalysts. *Appl. Catal. B* **2020**, *278*, 119315.
1033 [35] Khivantsev, K.; Jaegers, N.R.; Kovarik, L.; Wang, M.; Hu, J.Z.; Wang, Y.; Derewinski,
1034 M.A.; Szanyi, J. The superior hydrothermal stability of Pd/SSZ-39 in low temperature

1035 passive $NO_x$ adsorption (PNA) and methane combustion. *Appl. Catal. B* **2021**, *280*,
1036 119449.
1037 [36] Khivantsev, K.; Jaegers, N.R.; Kovarik, L.; Hu, J. Z.; Gao, F.; Wang, Y.; Szanyi, J.
1038 Palladium/zeolite low temperature passive $NO_x$ adsorbers (PNA): structure-adsorption
1039 property relationships for hydrothermally aged PNA materials. *Emiss. Contr. Sci. Tech.*
1040 **2020**, *6*, 126–138.
1041 [37] Castoldi, L.; Matarrese, R.; Morandi, S.; Ticali, P.; Lietti, L. Low-temperature Pd/FER
1042 $NO_x$ adsorbers: operando FT-IR spectroscopy and performance analysis. *Catal. Today*
1043 **2021**, *360*, 317–325.
1044 [38] Zhang, T.; Qiu, F.; Li, J. Design and synthesis of core-shell structured meso-Cu-SSZ-
1045 13@mesoporous aluminosilicate catalyst for SCR of $NO_x$ with $NH_3$: enhancement of
1046 activity, hydrothermal stability and propene poisoning resistance. *Appl. Catal. B* **2016**,
1047 *195*, 48–58.
1048 [39] Ye, Q.; Wang, L.; Yang, R.T. Activity, propene poisoning resistance and hydrothermal
1049 stability of copper exchanged chabazite-like zeolite catalysts for SCR of NO with
1050 ammonia in comparison to Cu/ZSM-5. *Appl. Catal. A* **2012**, *427–428*, 24–34.
1051 [40] Ogura, M.; Hayashi, M.; Kage, S.; Matsukata, M.; Kikuchi, E. Determination of active
1052 palladium species in ZSM-5 zeolite for selective reduction of nitric oxide with methane.
1053 *Appl. Catal. B* **1999**, *23*, 247–257.
1054 [41] Aylor, A.W.; Lobree, L.J.; Reimer, J.A.; Bell, A.T. Investigations of the dispersion of Pd
1055 in H-ZSM-5. *J. Catal.* **1997**, *172*, 453–462.
1056 [42] Yasumura, S.; Ide, H.; Ueda, T.; Jing, Y.; Liu, C.; Kon, K.; Toyao, T.; Maeno, Z.; Shimizu,
1057 K.-i. Transformation of bulk Pd to Pd cations in small-pore CHA zeolites facilitated by
1058 NO. *JACS Au* **2021**, *1*, 201–211.
1059 [43] Chen, D.; Lei, H.; Xiong, W.; Li, Y.; Ji, X.; Yang, J.-Y.; Peng, B.; Fu, M.; Chen, P.; Ye, D.
1060 Unravelling phosphorus-induced deactivation of Pd-SSZ-13 for passive $NO_x$ adsorption
1061 and CO oxidation. *ACS Catal.* **2021**, *11*, 13891–13901.

[44] Yao, D.; Feizie Ilmasani, R.; Wurzenberger, J.C.; Glatz, T.; Han, J.; Wang, A.; Creaser, D.; Olsson, L. Kinetic modeling of CO assisted passive $NO_x$ adsorption on Pd/SSZ-13. *Chem. Eng. J.* **2022**, *428*, 132459.

[45] Ambast, M.; Gupta, A.; Rahman, B.M.M.; Grabow, L.C.; Harold, M.P. $NO_x$ adsorption with CO and $C_2H_4$ on Pd/SSZ-13: experiments and modeling. *Appl. Catal. B* **2021**, *286*, 119871.

[46] Gu, Y.; Zelinsky, R.P.; Chen, Y.-R.; Epling, W.S. Investigation of an irreversible $NO_x$ storage degradation mode on a Pd/BEA passive $NO_x$ adsorber. *Appl. Catal. B* **2019**, *258*, 118032.

[47] Bian, C.; Li, D.; Liu, Q.; Zhang, S.; Pang, L.; Luo, Z.; Guo, Y.; Chen, Z.; Li, T. Recent progress of Pd/zeolite as passive $NO_x$ adsorber: adsorption chemistry, structure-performance relationships, challenges and prospects. *Chin. Chem. Lett.* **2022**, *33*, 1169–1179.

[48] Zhao, H.; Hill, A. J.; Ma, L.; Bhat, A.; Jing, G.; Schwank, J.W. Progress and future challenges in passive NO adsorption over Pd/zeolite catalysts. *Catal. Sci. Technol.* **2021**, *11*, 5986–6000.

[49] Smith, J.V.; Knowles, C.R.; Rinaldi, F. Crystal structures with a chabazite framework. III. Hydrated Ca-chabazite at +20 and −150 °C. *Acta Crystallogr.* **2010**, *17*, 374–384.

[50] Deka, U.; Lezcano-Gonzalez, I.; Weckhuysen, B.M.; Beale, A.M. Local environment and nature of Cu active sites in zeolite-based catalysts for the selective catalytic reduction of $NO_x$. *ACS Catal.* **2013**, *3*, 413–427.

[51] Higgins, J.B.; Lapierre, R.B.; Schlenker, J.L.; Rohrman, A.C.; Rohrbaugh, W.J. The framework topology of zeolite beta. *Zeolites* **1988**, *8*, 446–452.

[52] Jo, D.; Ryu, T.; Park, G.T.; Kim, P.S.; Kim, C.H.; Nam, I.-S.; Hong, S.B. Synthesis of high-silica LTA and UFI zeolites and $NH_3$-SCR performance of their copper-exchanged form. *ACS Catal.* **2016**, *6*, 2443–2447.

[53] Vaughan, P.A. The crystal structure of the zeolite ferrierite. *Acta Crystallogr.* **1966**, *21*.

[54] Okumura, K.; Amano, J.; Yasunobu, N.; Niwa, M. X-ray absorption fine structure study of the formation of the highly dispersed PdO over ZSM-5 and the structural change of Pd induced by adsorption of NO. *J. Phys. Chem. B* **2000**, *104*.

[55] Okumura, K.; Niwa, M. Regulation of the dispersion of PdO through the interaction with acid sites of zeolite studied by extended X-ray absorption fine structure. *J. Phys. Chem. B* **2000**, *104*, 9670–9675.

[56] Chen, Z.; Wang, M.; Wang, J.; Wang, C.; Wang, J.; Li, W.; Shen, M. Investigation of crystal size effect on the $NO_x$ storage performance of Pd/SSZ-13 passive $NO_x$ adsorbers. *Appl. Catal. B* **2021**, *291*, 120026.

[57] Lee, J.; Kim, J.; Kim, Y.; Hwang, S.; Lee, H.; Kim, C.H.; Kim, D.H. Improving $NO_x$ storage and CO oxidation abilities of Pd/SSZ-13 by increasing its hydrophobicity. *Appl. Catal. B* **2020**, *277*, 119190.

[58] Zhao, H.; Chen, X.; Bhat, A.; Li, Y.; Schwank, J.W. Understanding the chemistry during the preparation of Pd/SSZ-13 for the low-temperature NO adsorption: the role of $NH_4$-SSZ-13 support. *Appl. Catal. B* **2021**, *282*, 119611.

[59] Kovarik, L.; Washton, N.M.; Kukkadapu, R.; Devaraj, A.; Wang, A.; Wang, Y.; Szanyi, J.; Peden, C.H.F.; Gao, F. Transformation of active sites in Fe/SSZ-13 SCR catalysts during hydrothermal aging: a spectroscopic, microscopic, and kinetics study. *ACS Catal.* **2017**, *7*, 2458–2470.

[60] Ryu, T.; Ahn, N.H.; Seo, S.; Cho, J.; Kim, H.; Jo, D.; Park, G. T.; Kim, P. S.; Kim, C. H.; Bruce, E. L.; Wright, P. A.; Nam, I.-S.; Hong, S. B. Fully copper-exchanged high-silica LTA zeolites as unrivaled hydrothermally stable $NH_3$-SCR catalysts. *Angew. Chem. Int. Ed.* **2017**, *56*, 3256–3260.

[61] Khivantsev, K.; Wei, X.; Kovarik, L.; Jaegers, N.R.; Walter, E.D.; Tran, P.; Wang, Y.; Szanyi, J. Palladium/ferrierite versus palladium/SSZ-13 passive $NO_x$ adsorbers: adsorbate-controlled location of atomically dispersed palladium(II) in ferrierite determines high activity and stability. *Angew. Chem. Int. Ed.* **2022**, *61*, e202107554.

[62] Mihai, O.; Trandafilović, L.; Wentworth, T.; Torres, F.F.; Olsson, L. The effect of Si/Al ratio for Pd/BEA and Pd/SSZ-13 used as passive $NO_x$ adsorbers. *Top. Catal.* **2018**, *61*, 2007–2020.

[63] Mandal, K.; Gu, Y.; Westendorff, K. S.; Li, S.; Pihl, J. A.; Grabow, L.C.; Epling, W.S.; Paolucci, C. Condition-dependent Pd speciation and NO adsorption in Pd/zeolites. *ACS Catal.* **2020**, *10*, 12801–12818.

[64] Zhao, H.; Chen, X.; Bhat, A.; Li, Y.; Schwank, J. W. Insight into hydrothermal aging effect on deactivation of Pd/SSZ-13 as low-temperature NO adsorption catalyst: effect of dealumination and Pd mobility. *Appl. Catal. B* **2021**, *286*, 119874.

[65] Khivantsev, K.; Gao, F.; Kovarik, L.; Wang, Y.; Szanyi, J. Molecular level understanding of how oxygen and carbon monoxide improve $NO_x$ storage in palladium/SSZ-13 passive $NO_x$ adsorbers: the role of $NO^+$ and Pd(II)(CO)(NO) species. *J. Phys. Chem. C* **2018**, *122*, 10820–10827.

[66] Kim, Y.; Sung, J.; Kang, S.; Lee, J.; Kang, M.-H.; Hwang, S.; Park, H.; Kim, J.; Kim, Y.; Lee, E.; Park, G.-S.; Kim, D.H.; Park, J. Uniform synthesis of palladium species confined in a small-pore zeolite via full ion-exchange investigated by cryogenic electron microscopy. *J. Mater. Chem. A* **2021**, *9*, 19796–19806.

[67] Giordanino, F.; Borfecchia, E.; Lomachenko, K. A.; Lazzarini, A.; Agostini, G.; Gallo, E.; Soldatov, A.V.; Beato, P.; Bordiga, S.; Lamberti, C. Interaction of $NH_3$ with Cu-SSZ-13 catalyst: a complementary FTIR, XANES, and XES study. *J Phy. Chem. Lett.* **2014**, *5*, 1552–1559.

[68] Ryou, Y.; Lee, J.; Lee, H.; Kim, C. H.; Kim, D.H. Effect of various activation conditions on the low temperature NO adsorption performance of Pd/SSZ-13 passive $NO_x$ adsorber. *Catal. Today* **2019**, *320*, 175–180.

[69] Li, D.; Yang, G.; Chen, M.; Pang, L.; Guo, Y.; Yu, J.; Li, T. Na co-cations promoted stability and activity of Pd/SSZ-13 for low-temperature NO adsorption. *Appl. Catal. B* **2022**, *309*, 121266.

[70] Khivantsev, K.; Jaegers, N.R.; Kovarik, L.; Prodinger, S.; Derewinski, M.A.; Wang, Y.; Gao, F.; Szanyi, J. Palladium/Beta zeolite passive $NO_x$ adsorbers (PNA): clarification of PNA chemistry and the effects of CO and zeolite crystallite size on PNA performance. *Appl. Catal. A* **2019**, *569*, 141–148.

[71] Huang, S.; Wang, J.; Wang, J.; Wang, C.; Shen, M.; Li, W. The influence of crystallite size on the structural stability of Cu/SAPO-34 catalysts. *Appl. Catal. B* **2019**, *248*, 430–440.

[72] Albahar, M.; Li, C.; Zholobenko, V.L.; Garforth, A.A. The effect of ZSM-5 zeolite crystal size on p-xylene selectivity in toluene disproportionation. *Microporous Mesoporous Mater.* **2020**, *302*, 110221.

[73] Kwon, S.; Choi, Y.; Singh, B.K.; Na, K. Selective and rapid capture of $Sr^{2+}$ with LTA zeolites: effect of crystal sizes and mesoporosity. *Appl. Surf. Sci.* **2020**, *506*, 145029.

[74] Wen, F.; Ding, X.; Fang, X.; Liu, H.; Zhu, W. Crystal size sensitivity of HMOR zeolite in dimethyl ether carbonylation. *Catal. Commun.* **2021**, *154*, 106309.

[75] Wang, Y.; Gao, Y.; Chu, W.; Zhao, D.; Chen, F.; Zhu, X.; Li, X.; Liu, S.; Xie, S.; Xu, L. Synthesis and catalytic application of FER zeolites with controllable size. *J. Mater. Chem. A* **2019**, *7*, 7573–7580.

[76] Arévalo-Hidalgo, A.G.; Almodóvar-Arbelo, N.E.; Hernández-Maldonado, A.J. $Sr^{2+}$-SAPO-34 prepared via coupled partial detemplation and solid state ion exchange: effect on textural properties and carbon dioxide adsorption. *Ind. Eng. Chem. Res.* **2011**, *50*, 10259–10269.

[77] Vennestrøm, P.N.R.; Lundegaard, L.F.; Tyrsted, C.; Bokarev, D.A.; Mytareva, A.I.; Baeva, G.N.; Stakheev, A.Y.; Janssens, T.V.W. The role of protons and formation $Cu(NH_3)_2^+$ during ammonia-assisted solid-state ion exchange of copper(I) oxide into zeolites. *Top. Catal.* **2019**, *62*, 100–107.

[78] Shan, Y.; Sun, Y.; Li, Y.; Shi, X.; Shan, W.; Yu, Y.; He, H. Passive NO adsorption on hydrothermally aged Pd-based small-pore zeolites. *Top. Catal.* **2020**, *63*, 944–953.

[79] Bordiga, S.; Groppo, E.; Agostini, G.; van Bokhoven, J.A.; Lamberti, C. Reactivity of surface species in heterogeneous catalysts probed by in situ X-ray absorption techniques. *Chem. Rev.* **2013**, *113*, 1736–1850.

[80] Okumura, K.; Yoshimoto, R.; Uruga, T.; Tanida, H.; Kato, K.; Yokota, S.; Niwa, M. Energy-dispersive XAFS studies on the spontaneous dispersion of PdO and the formation of stable Pd clusters in zeolites. *J. Phys. Chem. B* **2004**, *108*, 6250–6255.

[81] Ryou, Y.; Lee, J.; Kim, Y.; Hwang, S.; Lee, H.; Kim, C. H.; Kim, D.H. Effect of reduction treatments ($H_2$ vs. CO) on the NO adsorption ability and the physicochemical properties of Pd/SSZ-13 passive $NO_x$ adsorber for cold start application. *Appl. Catal. A* **2019**, *569*, 28–34.

[82] Shimizu, K.-i.; Okada, F.; Nakamura, Y.; Satsuma, A.; Hattori, T. Mechanism of NO reduction by $CH_4$ in the presence of $O_2$ over Pd-H-Mordenite. *J. Catal.* **2000**, *195*, 151–160.

[83] Yu, Q.; Chen, X.; Bhat, A.; Tang, X.; Yi, H.; Lin, X.; Schwank, J.W. Activation of passive $NO_x$ adsorbers by pretreatment with reaction gas mixture. *Chem. Eng. J.* **2020**, *399*, 125727.

[84] Gupta, A.; Kang, S.B.; Harold, M.P. $NO_x$ uptake and release on Pd/SSZ-13: impact of feed composition and temperature. *Catal. Today* **2021**, *360*, 411–425.

[85] Vimont, A.; Thibault-Starzyk, F.; Daturi, M. Analysing and understanding the active site by IR spectroscopy. *Chem. Soc. Rev.* **2010**, *39*, 4928–4950.

[86] Khivantsev, K.; Jaegers, N. R.; Koleva, I.Z.; Aleksandrov, H.A.; Kovarik, L.; Engelhard, M.; Gao, F.; Wang, Y.; Vayssilov, G.N.; Szanyi, J. Stabilization of super electrophilic $Pd^{+2}$ cations in small-pore SSZ-13 zeolite. *J. Phys. Chem. C* **2020**, *124*, 309–321.

[87] Song, I.; Khivantsev, K.; Wang, Y.; Szanyi, J. Elucidating the role of CO in the NO storage mechanism on Pd/SSZ-13 with in situ DRIFTS. *J. Phys. Chem. C* **2022**, *126*, 1439–1449.

[88] Ma, Y.; Cheng, S.; Wu, X.; Shi, Y.; Cao, L.; Liu, L.; Ran, R.; Si, Z.; Liu, J.; Weng, D. Low-temperature solid-state ion-exchange method for preparing Cu-SSZ-13 selective catalytic reduction catalyst. *ACS Catal.* **2019**, *9*, 6962–6973.

[89] Lardinois, T. M.; Bates, J.S.; Lippie, H.H.; Russell, C.K.; Miller, J.T.; Meyer, H.M.; Unocic, K.A.; Prikhodko, V.; Wei, X.; Lambert, C.K.; Getsoian, A.B.; Gounder, R. Structural interconversion between agglomerated palladium domains and mononuclear Pd(II) cations in chabazite zeolites. *Chem. Mater.* **2021**, *33*, 1698–1713.

[90] Friberg, I.; Sadokhina, N.; Olsson, L. The effect of Si/Al ratio of zeolite supported Pd for complete $CH_4$ oxidation in the presence of water vapor and $SO_2$. *Appl. Catal. B* **2019**, *250*, 117–131.

[91] Pergher, S.B.C.; Dallago, R.M.; Veses, R.C.; Gigola, C.E.; Baibich, I.M. Pd/NaY-zeolite and Pd-W/NaY-zeolite catalysts: preparation, characterization and NO decomposition activity. *J. Mol. Catal. A: Chem.* **2004**, *209*, 107–115.

[92] Corma, A. Inorganic solid acids and their use in acid-catalyzed hydrocarbon reactions. *Chem. Rev.* **1995**, *95*.

[93] Choi, E.-Y.; Nam, I.-S.; Kim, Y.G. TPD study of mordenite-type zeolites for selective catalytic reduction of NO by $NH_3$. *J. Catal.* **1996**, *161*, 597–604.

[94] Villamaina, R.; Liu, S.; Nova, I.; Tronconi, E.; Ruggeri, M.P.; Collier, J.; York, A.; Thompsett, D. Speciation of Cu cations in Cu-CHA catalysts for $NH_3$-SCR: effects of $SiO_2/Al_2O_3$ ratio and Cu-loading investigated by transient response methods. *ACS Catal.* **2019**, *9*, 8916–8927.

[95] Wang, J.; Tang, J. Fe-based Fenton-like catalysts for water treatment: preparation, characterization and modification. *Chemosphere* **2021**, *276*, 130177.

[96] Roth, W.J.; Sasaki, T.; Wolski, K.; Ebina, Y.; Tang, D.-M.; Michiue, Y.; Sakai, N.; Ma, R.; Cretu, O.; Kikkawa, J.; Kimoto, K.; Kalahurska, K.; Gil, B.; Mazur, M.; Zapotoczny, S.; Čejka, J.; Grzybek, J.; Kowalczyk, A. Exfoliated ferrierite-related unilamellar nanosheets in solution and their use for preparation of mixed zeolite hierarchical structures. *J. Am. Chem. Soc.* **2021**, *143*, 11052–11062.

[97] Van der Mynsbrugge, J.; Head-Gordon, M.; Bell, A.T. Computational modeling predicts the stability of both $Pd^{+}$ and $Pd^{2+}$ ion-exchanged into H-CHA. *J. Mater. Chem. A* **2021**, *9*, 2161–2174.

[98] Mlekodaj, K.; Dedecek, J.; Pashkova, V.; Tabor, E.; Klein, P.; Urbanova, M.; Karcz, R.; Sazama, P.; Whittleton, S.R.; Thomas, H.M.; Fishchuk, A.V.; Sklenak, S. Al organization in the SSZ-13 zeolite. Al distribution and extraframework sites of divalent cations. *J. Phys. Chem. C* **2019**, *123*, 7968–7987.

[99] Göltl, F.; Müller, P.; Uchupalanun, P.; Sautet, P.; Hermans, I. Developing a descriptor-based approach for CO and NO adsorption strength to transition metal sites in zeolites. *Chem. Mater.* **2017**, *29*, 6434–6444.

[100] Aljama, H.A.; Head-Gordon, M.; Bell, A.T. Assessing the stability of Pd-exchanged sites in zeolites with the aid of a high throughput quantum chemistry workflow. *Nat. Commun.* **2022**, *13*, 2910.

[101] Wang, J.-g.; Liu, C.-j.; Fang, Z.; Liu, Y.; Han, Z. DFT study of structural and electronic properties of PdO/HZSM-5. *J. Phys. Chem. B* **2004**, *108*, 1653–1659.

[102] Che, M.; Dutel, J.F.; Gallezot, P.; Primet, M. A study of the chemisorption of nitric oxide on PdY zeolite. Evidence for a room temperature oxidative dissolution of palladium crystallites. *J. Phys. Chem.* **1976**, *80*, 2371–2381.

[103] Loffreda, D.; Simon, D.; Sautet, P. Structure sensitivity for NO dissociation on palladium and rhodium surfaces. *J. Catal.* **2003**, *213*, 211–225.

[104] Adelman, B. J.; Sachtler, W.M.H. The effect of zeolitic protons on $NO_x$ reduction over Pd/ZSM-5 catalysts. *Appl. Catal. B* **1997**, *14*, 1–11.

[105] Pommier, B.; Gelin, P. Infrared and volumetric study of NO adsorption on Pd-H-ZSM-5. *Phys. Chem. Chem. Phys.* **2001**, *3*, 1138–1143.

[106] Hadjiivanov, K.; Saussey, J.; Freysz, J.L.; Lavalley, J.C. FT-IR study of NO+$O_2$ co-adsorption on H-ZSM-5: re-assignment of the 2133 $cm^{-1}$ band to $NO^+$ species. *Catal. Lett.* **1998**, *52*, 103–108.

[107] Chen, D.; Yan, Y.; Guo, A.; Rizzotto, V.; Lei, H.; Qiao, Z.; Liang, H.; Jabłońska, M.; Jiang, X.; Jiang, J.; Palkovits, R.; Chen, P.; Ye, D.; Simon, U. Mechanistic insights into the promotion of low-temperature $NH_3$-SCR catalysis by copper auto-reduction in Cu-zeolites. *Appl. Catal. B* **2023**, *322*, 122118.

[108] Villamaina, R.; Iacobone, U.; Nova, I.; Tronconi, E.; Ruggeri, M.P.; Mantarosie, L.; Collier, J.; Thompsett, D. Mechanistic insight in NO trapping on Pd/chabazite systems for the low-temperature $NO_x$ removal from diesel exhausts. *Appl. Catal. B* **2021**, *284*, 119724.

[109] Lee, J.; Kim, Y.; Hwang, S.; Lee, E.; Lee, H.; Kim, C.H.; Kim, D.H. Deactivation of Pd/zeolites passive $NO_x$ adsorber induced by NO and $H_2O$: comparative study of Pd/ZSM-5 and Pd/SSZ-13. *Catal. Today* **2021**, *360*, 350–355.

[110] Ambast, M.; Karinshak, K.; Rahman, B.M.M.; Grabow, L.C.; Harold, M.P. Passive $NO_x$ adsorption on Pd/H-ZSM-5: experiments and modeling. *Appl. Catal. B* **2020**, *269*, 118802.

[111] Mei, D.; Gao, F.; Szanyi, J.; Wang, Y. Mechanistic insight into the passive $NO_x$ adsorption in the highly dispersed Pd/HBEA zeolite. *Appl. Catal. A* **2019**, *569*, 181–189.

[112] Lónyi, F.; Solt, H. E.; Valyon, J.; Decolatti, H.; Gutierrez, L.B.; Miró, E. An operando DRIFTS study of the active sites and the active intermediates of the NO-SCR reaction by methane over In,H- and In,Pd,H-zeolite catalysts. *Appl. Catal. B* **2010**, *100*, 133–142.

[113] Chakarova, K.; Ivanova, E.; Hadjiivanov, K.; Klissurski, D.; Knözinger, H. Co-ordination chemistry of palladium cations in Pd-H-ZSM-5 as revealed by FTIR spectra of adsorbed and co-adsorbed probe molecules (CO and NO). *Phys. Chem. Chem. Phys.* **2004**, *6*, 3702–3709.

[114] Kunal, P.; Toops, T.J.; Kidder, M.K.; Lance, M.J. Deactivation trends of Pd/SSZ-13 under the simultaneous presence of NO, CO, hydrocarbons and water for passive $NO_x$ adsorption. *Appl. Catal. B* **2021**, *299*, 120591.

[115] Vu, A.; Luo, J.; Li, J.; Epling, W.S. Effects of CO on Pd/BEA passive $NO_x$ adsorbers. *Catal. Lett.* **2017**, *147*, 745–750.

[116] Daldoul, I.; Chaouki, H.; Kaliaguine, S. Numerical study of the diffusion of binary hydrocarbon blends in ZSM-12 zeolites. *Micro. Mesoporous Mater.* **2018**, *256*, 49–57.

[117] Liu, C.; Wang, J.; Chen, Z.; Wang, J.; Shen, M. Improvement of $NO_x$ uptake/release over Pd/Beta by propylene: shielding effect of intermediates on adsorbed $NO_x$ species. *Phys. Chem. Chem. Phys.* **2021**, *23*, 5261–5269.

[118] Ambast, M.; Malamis, S.A.; Harold, M.P. Coupled uptake and conversion of $C_{12}H_{26}$ and NO on Pd/SSZ-13: experiments and modeling. *Chem. Eng. J.* **2021**, *423*, 129958.

[119] Savitz, S.; Siperstein, F.; Gorte, R.; Myers, A. Calorimetric study of adsorption of alkanes in high-silica zeolites. *J. Phys. Chem. B* **1998**, *102*.

[120] Azambre, B.; Westermann, A.; Finqueneisel, G.; Can, F.; Comparot, J.D. Adsorption and desorption of a model hydrocarbon mixture over HY zeolite under dry and wet conditions. *J. Phys. Chem. C* **2015**, *119*, 315–331.

[121] Guo, A.; Xie, K.; Lei, H.; Rizzotto, V.; Chen, L.; Fu, M.; Chen, P.; Peng, Y.; Ye, D.; Simon, U. Inhibition effect of phosphorus poisoning on the dynamics and redox of Cu active sites in a Cu-SSZ-13 $NH_3$-SCR catalyst for $NO_x$ reduction. *Environ. Sci. Technol.* **2021**, *55*, 12619–12629.

[122] Zhu, N.; Shan, W.; Shan, Y.; Du, J.; Lian, Z.; Zhang, Y.; He, H. Effects of alkali and alkaline earth metals on Cu-SSZ-39 catalyst for the selective catalytic reduction of $NO_x$ with $NH_3$. *Chem. Eng. J.* **2020**, *388*, 124250.

[123] Li, D.; Meng, Y.; Hao, D.; Ding, Q.; Pang, L.; Yang, G.; Guo, Y.; Yu, J.; Li, T. Deactivation of Pd/SSZ-13 passive $NO_x$ adsorber from the perspectives of phosphorus poisoning and hydrothermal aging. *Chem. Eng. J.* **2022**, *446*, 136779.

[124] Jia, Z.; Shen, Y.; Yan, T.; Li, H.; Deng, J.; Fang, J.; Zhang, D. Efficient NOx Abatement over Alkali-Resistant Catalysts via Constructing Durable Dimeric $VO_x$ Species. *Environ. Sci. Technol.* **2022**, *56*, 2647–2655.

[125] Fan, C.; Mi, J.; Wu, Q.; Chen, J.; Li, J. Deactivation of Pd/SSZ-13 by potassium and water for passive $NO_x$ adsorption. *Processes* **2022**, *10*, 222.

[126] Kim, Y.; Hwang, S.; Lee, J.; Ryou, Y.; Lee, H.; Kim, C. H.; Kim, D.H. Comparison of $NO_x$ adsorption/desorption behaviors over Pd/$CeO_2$ and Pd/SSZ-13 as passive $NO_x$ adsorbers for cold start application. *Emiss. Contr. Sci. Tech.* **2019**, *5*, 172–182.

[127] Mesilov, V.; Pon, L.; Dahlin, S.; Bergman, S.L.; Pettersson, L.J.; Bernasek, S.L. Computational study of noble metal CHA zeolites: NO adsorption and sulfur resistance. *J. Phys. Chem. C* **2022**, *126*, 7022–7035.

[128] Wang, A.; Xie, K.; Kumar, A.; Kamasamudram, K.; Olsson, L. Layered Pd/SSZ-13 with Cu/SSZ-13 as PNA–SCR dual-layer monolith catalyst for $NO_x$ abatement. *Catal. Today* **2021**, *360*, 356-366.

[129] Selleri, T.; Gramigni, F.; Nova, I.; Tronconi, E.; Dieterich, S.; Weibel, M.; Schmeisser, V. A PGM-free $NO_x$ adsorber + selective catalytic reduction catalyst system (AdSCR) for trapping and reducing $NO_x$ in lean exhaust streams at low temperature. *Catal. Sci. Technol.* **2018**, *8*, 2467–2476.

[130] Richard, P.; Richard, C.; Michael, G.; Eben, H.; Alexander, W.; Miroslaw, G.; Adam, B. Combining SCR with PNA for low temperature emission control. US 2016/0136626 A1, 2016.

[131] Kim, M.-S.; Lee, D.-W.; Chung, S.-H.; Hong, Y.-K.; Lee, S. H.; Oh, S.-H.; Cho, I.-H.; Lee, K.-Y. Oxidation of ammonia to nitrogen over Pt/Fe/ZSM5 catalyst: influence of catalyst support on the low temperature activity. *J. Hazard. Mater.* **2012**, *237–238*, 153–160.

[132] Chen, H.-Y.; Kilmartin, J.; Liu, D.; Lu, J.; Duran-Martin, D.; Rajaram, R. A. J. Catalytic article comprising a platinum group metal and base metal on a molecular sieve for PNA-ASC close-coupled systems. EP 3600626 B1, 2021.

[133] Chen, H.-Y.; Fedeyko, J.; Liu, D.; Lu, J. Single brick SCR/ASC/PNA/DOC close-coupled catalyst. GB 2571640 B, 2021.

[134] Robert, T.; Kay, L.; Allen, D. Emissions reduction system. US 9657626 B2, 2017.

[135] Conway, R.; Aydin, C.; Chatterjee, S.; Naseri, M. Increased $NO_x$ conversion by ozone introduction. EP 3555437 A1, 2019.

[136] Bergeal, D.; Dunkley, N.; Hatcher, D.; Izzard, A.; Phillips, P. In-exhaust electrical element for $NO_x$ storage catalyst and SCR systems. WO 2017/168156 A1, 2017.

[137] Zhang, C.; Zhang, J.; Shen, Y.; He, J.; Qu, W.; Deng, J.; Han, L.; Chen, A.; Zhang, D. Synergistic catalytic elimination of $NO_x$ and chlorinated organics: cooperation of acid sites. *Environ. Sci. Technol.* **2022**, *56*, 3719–3728.

[138] Xiong, W.; Liu, L.; Guo, A.; Chen, D.; Shan, Y.; Fu, M.; Wu, J.; Ye, D.; Chen, P. Economical and sustainable synthesis of small-pore chabazite catalysts for $NO_x$ abatement by recycling organic structure-directing agents. *Environ. Sci. Technol.* **2023**, *57*, 655–665.

[139] Crehan, G. System and method for regenerating a nitrogen oxides adsorber. WO 2015/001221 A1, 2015.

[140] Chen, Z.; Bian, C.; Guo, Y.; Pang, L.; Li, T. Efficient strategy to regenerate phosphorus-poisoned Cu-SSZ-13 catalysts for the $NH_3$-SCR of $NO_x$: the deactivation and promotion mechanism of phosphorus. *ACS Catal.* **2021**, *11*, 12963–12976.

[141] Jangjou, Y.; Do, Q.; Gu, Y.; Lim, L.-G.; Sun, H.; Wang, D.; Kumar, A.; Li, J.; Grabow, L.C.; Epling, W.S. Nature of Cu active centers in Cu-SSZ-13 and their responses to $SO_2$ exposure. *ACS Catal.* **2018**, *8*, 1325–1337.

[142] Dudar, A. Systems and methods for reducing vehicle emissions. US 10563605 B2, 2020.

[143] Zhang, X. Emissions control during engine cold starts. US 11193438 B1, 2021.

[144] Leone, T.; Vanderwege, B.A.; Moilanen, P.C.; Zhang, X. Systems and methods for hot air injection into exhaust ports. US 2022/0145790 A1, 2022.

[145] Harris, T.; Mc Pherson, K.; Rezaei, R.; Kovacs, D.; Rauch, H.; Huang, Y. Modeling of close-coupled SCR concepts to meet future cold start requirements for heavy-duty engines. *SAE Technical Paper* **2019**, 2019-01-0984.